



Cu-doped CoOOH activates peroxyomonosulfate to generate high-valent cobalt-oxo species to degrade organic pollutants in saline environments

Yufei Han^{a,b}, Chuanfu Zhao^{b,c}, Wenchao Zhang^{b,c}, Zhe Liu^{a,b}, Zhe Li^{b,c}, Fei Han^{b,c}, Mengru Zhang^{b,c}, Fei Xu^d, Weizhi Zhou^{b,c,*}

^a School of Environmental Science and Engineering, Shandong University, Qingdao, Shandong 266000, China

^b Laboratory of Water-Sediment Regulation and Eco-decontamination, Jinan, Shandong 250000, PR China

^c School of Civil Engineering, Shandong University, Jinan, Shandong 250000, China

^d Environment Research Institute, Shandong University, Jinan, Shandong University, Qingdao, Shandong 266000, China



ARTICLE INFO

Keywords:

Peroxyomonosulfate

Selectivity

Saline wastewater

DFT calculation

High-valent cobalt-oxo species

ABSTRACT

A Cu doped CoOOH-activated peroxyomonosulfate (CoCu10/PMS) process was developed to enable the generation of Co(IV)=O for efficient oxidation of pollutants in saline water. The formation of Co(IV)=O was demonstrated through phenylmethyl sulfoxide (PMSO) probe and ¹⁸O-isotope-labeling tests. CoCu10 was synthesized using a simple and scalable co-precipitation method, enabling efficient synthesis at laboratory scale for large quantities (gram level). Cu doping increased the surface hydroxyl density of CoOOH, thereby improving its activation performance. Coordinating with PMS through surface hydroxyls, CoCu10 formed catalyst-PMS complexes, then donated electrons to induce heterolytic cleavage of O-O bonds in complexes, resulting in the formation of Co(IV)=O. At a concentration of 0.2 g/L catalyst and 0.2 mM PMS, 97.7% of tetracycline was degraded within 10 min. CoCu10 maintained stable performance over eight cycles. Thanks to Co(IV)=O, the CoCu10/PMS system efficiently operates under different concentrations of Cl⁻, HCO₃⁻, NO₃⁻, SO₄²⁻, H₂PO₄⁻ and mixed salt.

1. Introduction

Efficiently removing residual organic pollutants from the hydro-sphere is crucial as even low concentrations of pollutants can pose a serious ecological hazard [1]. Among the numerous types of organic pollutants, the antibiotics in aquatic environments has emerged as a global concern, presenting significant potential risks to both human health and environmental safety. Tetracycline (TC), as a typical antibiotic, is widely detected in various water environments [2]. The rapid and efficient removal of TC is a challenging task due to its resistance to conventional wastewater treatment methods [3]. The sulfate radical-advanced oxidation process (SR-AOP) is widely considered an effective method for rapidly removing TC and other organic pollutants due to the production of reactive oxygen species (ROS) with high redox potential, including sulfate radicals (SO₄²⁻), hydroxyl radicals (•OH), singlet oxygen (¹O₂), high-valanced metal-oxo species (HVMS) and others [4]. The activation of peroxyomonosulfate (PMS) or persulfate (PS) is crucial in this oxidation process, and catalysts play a key role in determining its performance. Therefore, laboratory-scale pollutant

degradation is a key focus in current SR-AOP-oriented researches, and the activation performance of catalysts in deionized water can be well evaluated by the degradation efficiency of pollutants [5]. However, the coexistence of inorganic anions in real wastewater remains a highly challenging issue for practical applications. These inorganic anions can have various adverse effects on the SR-AOPs process. Firstly, some anions (e.g., Cl⁻, HCO₃⁻, NO₃⁻, SO₄²⁻ and H₂PO₄⁻) can react rapidly with some radicals (e.g., SO₄²⁻ and •OH) to form secondary anion radicals with lower oxidation ability, which severely inhibits the degradation of target pollutants [6]. Furthermore, some secondary radicals, such as chlorine and nitrate radicals (Cl[•] and NO₃[•]), may react with organics in water to generate chlorinated and nitrated byproducts, posing potential environmental risks [7]. In light of the above points, it is crucial to give due consideration and address the stress imposed by anions on the reaction process in an SR-AOPs system.

The various contradictions brought about by anions can be well alleviated by the non-radical activation pathway of SR-AOPs [8]. HVMS, as a non-radical pathway, can avoid interference by anions while focusing on the degradation of targeted pollutants, thanks to its

* Corresponding author.

E-mail address: wzzhou@sdu.edu.cn (W. Zhou).

unparalleled selectivity [9]. In fact, beyond the SR-AOPs field, HVMS has been widely studied and used as a reaction intermediate for C–H activation, alkene epoxidation, and oxygen atom transfer reactions due to its excellent oxidation ability and selectivity [10]. However, in the field of SR-AOPs, the understanding of other HVMS such as Co(IV) is still quite limited, apart from Fe(IV). In fact, due to the presence of the oxo-wall between iron-group and cobalt-group metals, the reactivity of Co(IV) is stronger than other commonly encountered HVMS such as Fe(IV) and Mn(III) [11]. Due to the strong electronic repulsion between the d-orbitals of the transition metals and the p-orbitals of oxo, the HVMS after the iron-group, including Co, are extremely unstable and highly reactive [12]. Perhaps in the field of organic synthesis, the instability and high reactivity of Co(IV) prevent it from being used to continuously and stably oxidize substrates [13]. However, in the field of SR-AOPs, these characteristics mean that it can degrade target organic compounds more quickly and thoroughly than other HVMS. Unfortunately, the current understanding on Co(IV) is relatively limited in field of SR-AOPs, with most studies focusing on homogeneous rather than heterogeneous catalysis, and there have been few investigations into the selectivity and reactivity of Co(IV) in wastewater with background impurities [14,15].

While it has been reported that homogeneous cobalt SR-AOPs can produce a certain amount of Co(IV), they also have some inherent drawbacks that cannot be overcome, such as activity decay, sludge generation, pH dependence and biotoxicity [16]. These limitations make it challenging to further promote the use of homogeneous cobalt SR-AOPs. However, heterogeneous SR-AOPs offer a promising solution as they can effectively mitigate above issues and provide a more viable alternative. Currently, several heterogeneous Co(IV)=O-based catalysts have been developed, including nitrogen-fixing cobalt single atoms catalyst, cobalt-doped C_3N_5 and so on [15,17]. These catalysts share a common feature, namely that they are all Co–CN catalysts. However, other studies have suggested that Co–CN catalysts may have a greater propensity to induce the generation of other ROS (such as SO_4^{2-} and O_2^{\cdot}) rather than Co(IV)=O [15]. In other words, the electronic structure of Co–CN catalysts is uncontrollable, which can affect the reaction barrier and make the activation pathway for oxidants unpredictable. Moreover, Co–CN catalysts face several engineering challenges, including low yields, high synthesis difficulty and high cost.

Based on the aforementioned discussion, it is imperative to find a PMS catalyst that can be synthesized in a simple and extensible method, and is capable of generating Co(IV)=O as the dominated ROS. We turn our attention to cobalt hydroxide (CoOOH). CoOOH is a cobalt oxide with highly controllable structure and chemical properties and it can be synthesized by a large-scale synthesis of the co-precipitation method, which has cost benefits [18,19]. Due to these advantages, CoOOH-based materials have been widely used as catalysts for oxygen evolution reaction (OER), and the Co(IV) has been confirmed to be the main active species of CoOOH in OER [20,21]. According to reports, the interaction process between PMS and the catalyst is very similar to the oxidation reaction process that occurs at the anode of OER [22,23]. Inspired by the OER process, it seems feasible to generate Co(IV)=O from CoOOH under the action of PMS. In addition, the prerequisite for the formation of HVMS is the formation of catalyst-PMS complexes between PMS and metal sites, and the abundant surface hydroxyls of CoOOH undoubtedly provide sufficient sites for the formation of Co(IV)=O [22]. However, a negative issue also urgently needs to be solved simultaneously: the poor activation performance of CoOOH for PMS cannot meet the application requirements, which has been confirmed by some reports and our previous work [24,25]. Fortunately, many reports have confirmed that the substitution of Co atoms with a very small amount of transition metals with similar radii (e.g., Cu and Fe) can greatly improve the performance of CoOOH in various applications, such as OER and HER [26,27]. Therefore, the use of Cu doping is also expected to enhance the activation performance of CoOOH for PMS. Therefore, the purpose of this work is to explore: 1). whether a small amount of Cu doping could

enhance the activation performance of CoOOH for PMS. 2). what is the mechanism of Cu-doped CoOOH to activate PMS? 3). whether the dominant ROS in Cu-doped CoOOH/PMS system is Co(IV)=O. 4). whether the Cu doped CoOOH/PMS system can operate efficiently in various anionic background.

2. Materials and methods

2.1. Chemicals and reagents

The reagents used in the experiment are analytical pure and can be used directly without further purification. All reagents used in this work are described in the Text S1 of [Supplementary Material](#).

2.2. Synthesis of materials

The Cu-doped CoOOH was synthesized via a classical co-precipitation-oxidation method. In a typical process, 100 ml of an 8.4 g/L NaOH solution was added dropwise to a solution containing 50 ml of x M Co^{2+} and $1 - x$ M Cu^{2+} , and the mixture was stirred for 30 min to ensure complete reaction. Subsequently, 30 ml of hydrogen peroxide solution was slowly added and the resulting mixture was placed in a water bath shaker, oscillated at 200 rpm for 24 h at 60 °C. Finally, the mixture was filtered and washed three times to obtain a sample of Cu-doped CoOOH, named CoCux, where x represents the atomic ratio of Cu in the sample.

The actual atomic ratio of CoCux was determined using ICP-OES, as presented in [Table S1](#). The results obtained from ICP-OES were found to be in close agreement with the theoretical ratio, thereby confirming that Co was fully integrated into the structure of CoOOH.

2.3. Characterization

XRD, FTIR, Raman, SEM, TEM, XPS and some other characterization methods have been used to characterize the physical and chemical properties of the samples. Detailed information on characterization could be found in the Text S2 of [Supplementary Material](#).

2.4. Experimental procedure

Details on the experimental procedures can be found in the Text S3 of the [Supplementary Material](#).

2.5. Analytical and experimental methods

Details on the analytical methods (Text S4), Rietveld structure refinement (Text S5), ^{18}O -isotope-labeling experiment (Text S6), activated sludge inhibition experiment (Text S7) and DFT calculation (Text S8) can be found in the [supplementary material](#).

3. Results and discussion

3.1. Characterization

The crystal structures of the synthesized samples were characterized utilizing X-ray diffraction (XRD) analysis. As depicted in [Fig. 1a](#), the diffraction peaks of CoOOH were found to be consistent with the PDF-#73-0497 pattern, signifying the successful synthesis of CoOOH [28]. The XRD patterns of the Cu-doped samples were in close agreement with those of the pure CoOOH, with no evidence of new phases being present. However, with the increment of Cu doping, a notable decrease in the intensity of the diffraction peaks was observed, suggesting a rise in the degree of lattice disorder and a decrease in the crystallinity of the samples. Moreover, it was noted that the (003) and (015) peaks shifted towards lower angles as the Cu incorporation increased ([Fig. 1b](#)), which signifies an increase in the cell parameters of CoOOH as a result of the

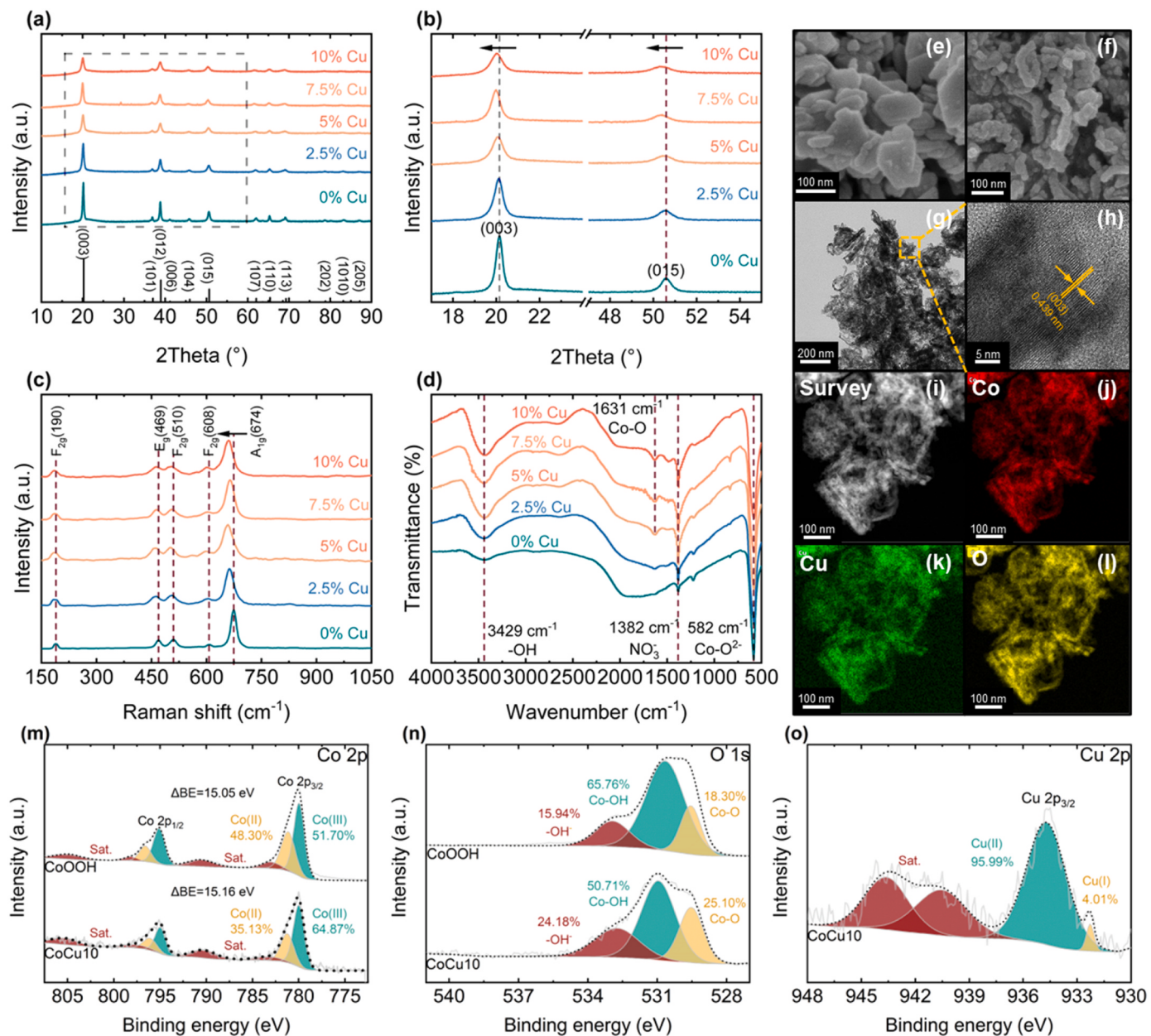


Fig. 1. XRD (a, b), Raman (c) and FTIR (d) spectra of several samples. SEM images of CoOOH and CoCu10 (e, f). TEM images (g, h) of CoCu10. EDS mapping images (i, j, k, l) of CoCu10. XPS Co 2p (m), O 1s (n), Cu 2p (o) deconvolution of CoCu10.

incorporation of Cu. The Rietveld structure refinement of CoCu10 and CoOOH confirmed this observation. For CoCu10, we set Cu at the Co sites and finally achieved convergence. The *R*-factors of CoCu10 and CoOOH indicates that the refinement results are reliable, as shown in Table 1 and Fig. S1. Compared with CoOOH, the introduction of Cu led to a slight increase in the lattice parameters, *a* and *b* slightly increased from 2.8545 Å to 2.8567 Å, and *c* (layer spacing) increased from 13.1366 Å to 13.2161 Å. The corresponding cell volume also increased from 92.700 Å³ to 93.400 Å³, and the grain size decreased from 69.822

nm to 23.731 nm. These changes are due to the slight expansion of the unit cell due to the slightly larger radius of the Cu²⁺ ions than the Co³⁺ ions, suggesting the substitutional doping of Cu into the Co sites. In addition, due to the larger ionic radius, Cu²⁺ ions cannot smoothly incorporate into the system and occupy the interstitial positions in theory, so the interstitial doping of Cu can be definitely ruled out.

In order to conduct a comprehensive analysis of the crystal structure, Raman spectrum was employed to characterize the sample. Fig. 1c demonstrates that CoOOH displays a total of five distinct phonon modes,

Table 1
Refined unit cell parameters of CoOOH and CoCu10.

Samples	Space group	<i>a</i> (Å)	<i>b</i> (Å)	<i>c</i> (Å)	Volume (Å ³)	Grain size (nm)	<i>R</i> _{wp} (%)	<i>R</i> _p (%)
CoOOH	R-3 m	2.8545	2.8545	13.1366	92.700	69.822	1.24	0.92
CoCu10	R-3 m	2.8567	2.8567	13.2161	93.400	23.731	0.98	0.76

including F_{2g} (190 cm^{-1}), E_g (496 cm^{-1}), F_{2g} (510 cm^{-1}), F_{2g} (608 cm^{-1}), and A_{1g} (674 cm^{-1}) [29]. The Raman shifts observed at 190 , 510 , and 608 cm^{-1} could be attributed to the asymmetrical vibrations of the O–O, O–Co–O, and Co–O bonds, respectively, within CoOOH. The characteristic peaks observed at 496 and 674 cm^{-1} result from the symmetrical vibrations of the O–O and O–H bonds in the sample. Despite varying levels of Cu doping, Cu-doped CoOOH retains the basic Raman spectrum pattern of CoOOH, further confirming that the addition of Cu did not lead to the formation of new phases. Notably, the peak at 674 cm^{-1} underwent a significant red shift with increasing levels of Cu doping, indicating an increase in the length of the O–H bond, which suggests increased activity of the surface hydroxyl groups in the sample. In addition to the peak at 674 cm^{-1} , a slight red shift could also be observed in other peaks, indicating that Cu doping overall made CoOOH more unstable, which is undoubtedly beneficial for catalytic reactions [30].

As depicted in Fig. 1d, the functional groups present at the surface of the sample were analyzed utilizing FTIR. The absorption peaks observed at approximately 582.9 , 1631.0 , and 3429.4 cm^{-1} correspond to the Co–O²⁻, Co–O, and –OH bonds present in CoOOH, respectively [31]. An absorption peak observed at $\sim 1382.0\text{ cm}^{-1}$ indicates the presence of residual nitrates, which is a consequence of utilizing nitrates in the synthesis process. Upon comparing the spectra of samples with varying Cu content, it was noted that the strength of the Co–O bond increased with an increase in the Cu content. This phenomenon can be attributed to the interaction between Cu and Co atoms, which influences the strength of the Co–O bond [27]. Although peaks related to Cu–O bonds are usually observed near 600 cm^{-1} , close to the position of the Co–O²⁻ peak, they were not detected in this research. This may be attributed to the Co–O²⁻ peak obscuring it. Additionally, the intensity of the –OH bond showed an increase with the addition of Cu, implying an augmentation in the density of surface hydroxyl groups.

The morphology and structure of CoOOH and CoCu10 were studied utilizing SEM. As demonstrated in Fig. 1e, CoOOH exhibits a typical and irregular stacked plate morphology, with an average diameter of approximately 100 nm . Upon the incorporation of Cu, however, the plate structure was transformed into nearly spherical nanoparticle nanoparticles of smaller size, with a size range between 10 and 30 nm (Fig. 1f). This transformation in the morphology and dimension of CoCu10 is undoubtedly advantageous for the catalytic reaction as it could augment the surface area of samples in contact with medium. HRTEM further showed that the addition of Cu resulted in a significant decrease in the crystallinity of CoCu10 and a highly disordered lattice arrangement (Fig. 1g), which was consistent with the findings from XRD. This phenomenon implies that the incorporation of Cu has resulted in a significant number of defects in the structure of CoCu10. From Fig. 1h, it can be observed that there are lattice fringes with a spacing of 0.439 nm , which corresponds to the (003) plane of CoCu10. Additionally, the results from EDS mapping confirmed the uniform distribution of Co, Cu, and O elements in CoCu10 (as depicted in Fig. 1i-l).

In order to distinguish the differences in chemical composition and oxidation state between CoOOH and CoCu10, XPS analysis was conducted. (Survey spectra were shown in Fig. S2). As depicted in Fig. 1m, the Co 2p spectra of both samples could be attributed to the Co 2p_{3/2} and Co 2p_{1/2} peaks, which are situated around 780 and 795 eV . The span splitting (ΔBE) between the two peaks in CoOOH was found to be 15.05 eV , which agrees with the standard ΔBE of CoOOH ($15.0 \pm 0.1\text{ eV}$) [25]. Notably, the ΔBE of CoCu10 increased to 15.16 eV , indicating that the presence of Cu doping leads to a transformation of some Co(II) to Co(III) in CoOOH. This was further confirmed by the deconvolution of the Co 2p region, with the peaks at 780.02 and 781.30 eV being assigned to Co(III) and Co(II). The Co(III) content in CoOOH was 51.70% , while it increased to 64.87% in CoCu10, which may be attributed to the change of the coordination environment of Co atoms by the introduction of Cu atoms.

Additionally, the introduction of Cu into the samples had a

significant impact on the oxygen species present on the surface of samples. As depicted in Fig. 1n, the O1s spectra of both samples could be decomposed into three peaks located at 532.7 eV , 530.9 eV , and 529.5 eV , respectively, corresponding to surface hydroxyls ($-\text{OH}^-$), lattice hydroxyls (Co–OH), and lattice oxygen (Co–O). The results indicate that the doping of Cu significantly altered the proportion of the three oxygen species, for instance, the relative proportion of lattice hydroxyl decreased from 65.76% to 50.71% , implying a decrease in catalyst crystallinity, which is consistent with the XRD results mentioned earlier. It is noteworthy that the proportion of surface hydroxyl ($-\text{OH}^-$) increases from 15.94% to 24.18% , which is also reflected in the FTIR results presented earlier. This increase in the density of surface hydroxyls has been linked to the catalytic activity of metal oxides, as they can act as acidic intermediates to enhance catalytic reactions [32]. In particular, surface hydroxyls have been identified as important sites in the activation of some metal oxides for PMS, responsible for capturing HSO_5^- from the medium and transferring it to the surface of the catalyst [33,34]. Thus, the increased density of surface hydroxyls brought about by Cu doping may have a positive impact on the activation effect of CoOOH on PMS.

The Cu 2p XPS spectrum, as depicted in Fig. 1o, exhibits a binding energy of 934.6 eV for the Cu 2p_{3/2} orbital. Studies have revealed that the binding energy of Cu(II) typically falls within a range of 933.5 – 934.8 eV , whereas the peak position of Cu(I) and Cu⁰ is generally around 932.5 eV [35]. Based on this information, it could be deduced that the majority of Cu in the CoCu10 sample exists in the form of Cu(II). This conclusion is further supported by the results of the Cu 2p spectrum deconvolution, which shows that the Cu 2p_{3/2} peak is divided into two peaks, with Cu(II) at 934.7 eV accounting for 95.99% and Cu(I) at 932.3 eV accounting for a mere 4.01% . This observation could be attributed to the continuous oxidation by oxidizing agents (hydrogen peroxide and oxygen) during the synthesis of the CoCu10 sample.

The BET specific surface areas of CoOOH and CoCu10 were measured by the analysis of nitrogen adsorption-desorption isotherms performed at 77 K , as depicted in Fig. S3. Both samples displayed a type-IV isotherm and H3 hysteresis loop, indicating that the porosity of CoOOH and CoCu10 predominantly consists of mesopores with an irregular shape [36]. The pore size distribution of CoOOH and CoCu10, as depicted in illustration, primarily ranges from 2 to 50 nm , which, according to the definition of IUPAC, classifies both catalysts as mesoporous materials. The BET surface area, pore volume, and average pore size of CoOOH were found to be $21.9276\text{ m}^2/\text{g}$, $0.052931\text{ cm}^3/\text{g}$, and 9.6556 nm , respectively, while the corresponding values for CoCu10 were $78.3780\text{ m}^2/\text{g}$, $0.183821\text{ cm}^3/\text{g}$, and 9.3812 nm . In comparison to CoOOH, CoCu10 displayed significantly increased BET surface area and pore volume, which could be attributed to the reduction in particle size resulting from Cu doping, as evidenced by the SEM characterization results above. The enhanced surface area and pore volume could increase the contact area between CoCu10 and the reaction medium, thereby facilitating faster adsorption of PMS or pollutants onto the material surface and accelerating the catalytic reaction.

The electron transfer rate is a crucial factor in catalytic reactions, and this could commonly be measured using EIS. Based on the observations presented in Fig. S4, it is clear that the Nyquist semicircle exhibited by CoCu10 in the high-frequency region has a smaller radius than that of CoOOH, which implies that CoCu10 has a stronger electron transfer ability than CoOOH. In addition, it has been reported that the doping of transition metals may result in the generation of oxygen vacancies, thereby leading to a significant influence on the catalytic performance and mechanisms of metal oxides [37,38]. EPR was employed to identify potential oxygen vacancies in CoOOH and CoCu10. As shown in Fig. S5, neither material exhibited distinct identifiable signals, indicating the absence of oxygen vacancies in CoOOH and CoCu10. Therefore, potential influences of oxygen vacancies on the performance or mechanisms of CoCu10 can be ruled out.

3.2. Activation performance of the catalyst

Firstly, the influence of Cu doping on the activation performance of catalysts was assessed, and TC was employed as a probe pollutant. The results, depicted in Fig. S6a, clearly demonstrate that the activation performance of the catalysts for PMS progressively enhanced with an increase in Cu doping. Even a minute Cu doping level, such as 2.5%, significantly enhanced the activation performance of CoOOH, elevating the TC removal from 46.6% to 90.1%. Moreover, as depicted in Fig. S6b, the k_{obs} of the four Cu-doped samples exhibit an ascending order of 0.3839, 0.4879, 0.5851, and 0.6482 min⁻¹, displaying an excellent linear correlation with the amount of Cu doping (Fig. S6c). As CoCu10 exhibited the best activation performance, this sample was chosen for the subsequent experiments.

The degradation performance of different reaction systems on TC was also compared. As shown in Fig. 2a, the CoCu10/PMS process removed approximately 97.6% of TC within 10 min. The fact that only about 14% and 36% of TC were reduced in sole PMS and CoCu10, respectively, indicates that sole PMS cannot effectively oxidize TC and that the adsorption of CoCu10 is not the main reason for the rapid removal of TC. Additionally, CoOOH did not exhibit the ideal activation performance for PMS, under the same conditions, only 46.5% of TC was reduced by the CoOOH/PMS process. As shown in Fig. S7, the apparent rate constants (k_{obs}) for PMS, CoCu10, CoOOH/PMS, and CoCu10/PMS are 0.0143, 0.0532, 0.0668, and 0.6482 min⁻¹, respectively. Compared to the original CoOOH, Cu doping led to a tenfold improvement in its activation performance for PMS.

The removal effects of CoCu10/PMS and CoOOH/PMS on TOC were

also evaluated. As illustrated in Fig. S8, in the CoCu10/PMS system, 51.5% of TOC was rapidly removed within 10 min, and with an extended reaction time of 60 min, the TOC removal eventually reached 60.7%. In contrast, the performance of the CoOOH/PMS system in terms of TOC removal was unsatisfactory, with only 10.4% removed within 10 min and 27.2% within 60 min. This result indicates that the CoCu10/PMS process has great potential for practical application.

Another important indicator for evaluating the activation performance of a catalyst is the reaction stoichiometric efficiency (RSE). In SR-AOPs systems, RSE is defined as the number of moles of pollutants oxidized for every mole of PMS activated in the presence of catalyst in a given time period [39]. In view of this, the decomposition of PMS in the CoCu10/PMS system was measured, and it was found that PMS was rapidly decomposed by 54.3% within 10 min (Fig. S9), which once again demonstrated the strong activation performance of CoCu10 on PMS. The RSE of the CoCu10/PMS system was calculated to be 20%, far surpassing other SR-AOPs systems that have been reported to use TC as a probe pollutant (Fig. 2b and Table S2).

The influence of catalyst dosage on the performance of the CoCu10/PMS process was examined. As illustrated in Fig. S10a, an increase in the catalyst dosage could result in an improvement in TC removal efficiency in the system. The corresponding k_{obs} increased from 0.4534 min⁻¹ to 3.0580 min⁻¹ as the dosage increased from 0.05 g/L to 1.00 g/L (Fig. S10b). At a catalyst dosage of 1.00 g/L, TC in the system was completely degraded within 2 min, showing the powerful performance of the CoCu10/PMS process. However, an increase in catalyst dosage also implies the increase in leaching hazard and treatment costs, and excessively rapid reaction rate may bring difficulties to the exploration

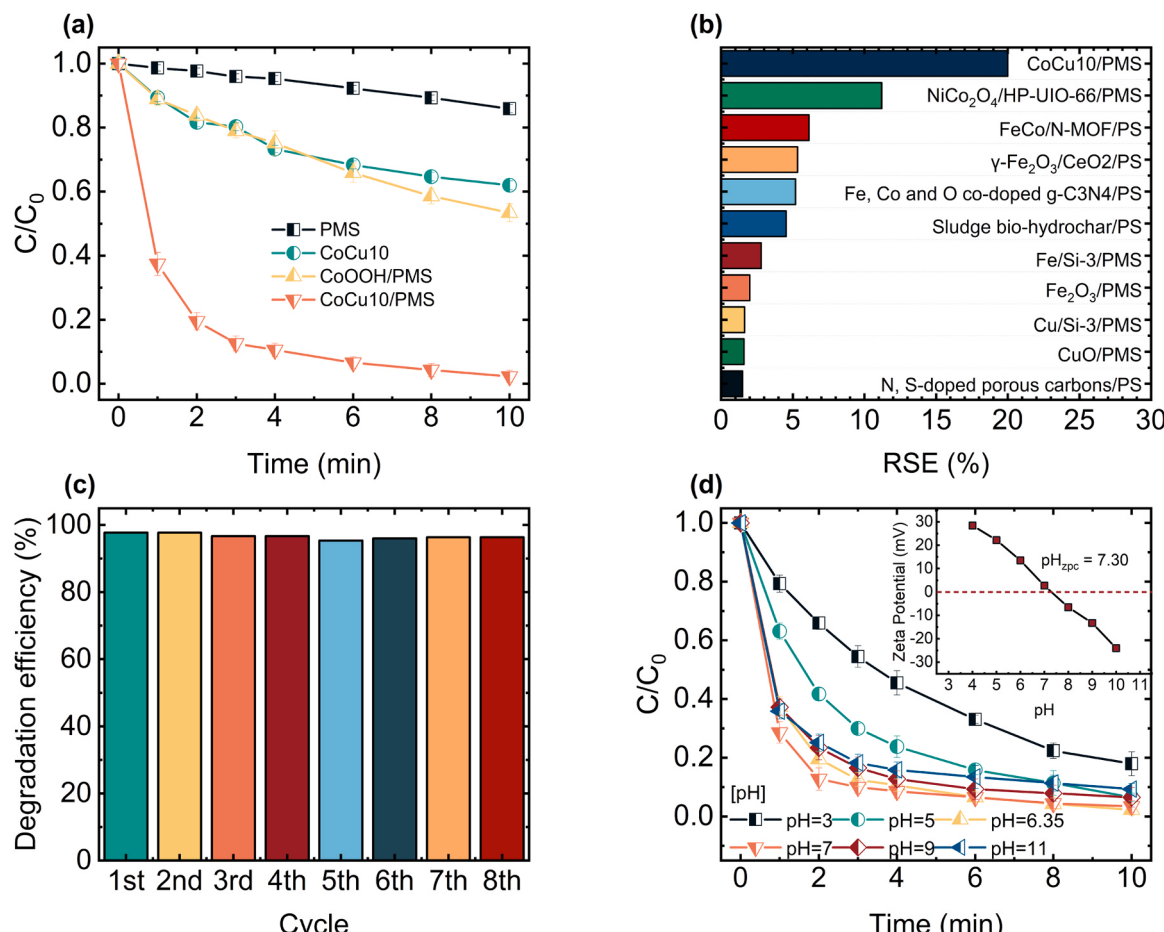


Fig. 2. (a) The performance of different systems. (b) RSE of different SR-AOPs systems, and the references can be found in Table S2 in the supplementary material. (c) Reuse performance of CoCu10. (d) Effect of initial pH on the performance of CoCu10/PMS system, the illustration is the zeta potential of CoCu10 at different pH. Reaction conditions: [TC] = 22.5 μ M, [Catalyst] = 0.05–0.50 g/L, [PMS] = 0.05–0.5 mM, [Temperature] = 15–45 °C and [initial pH] = 3–11.

of the reaction mechanism. Therefore, considering factors such as costs, potential environmental hazard, and exploration of the mechanism, we have chosen a catalyst dosage of 0.20 g/L for the subsequent experiments.

The influence of PMS concentration on the CoCu10/PMS process is presented in Fig. S11a. Within the range of 0.05–0.3 mM, the removal of TC by CoCu10/PMS increased with the increase in PMS concentration. Correspondingly, the k_{obs} increased from 0.5520 min^{-1} to 0.7178 min^{-1} (Fig. S11b). Notably, even at an ultra-low PMS concentration of 0.05 mM, the CoCu10/PMS process was capable of removing approximately 88.9% of TC within 10 min, demonstrating the strong activation performance of CoCu10 for PMS. Within this range, the k_{obs} exhibited an overall positive correlation with PMS concentration, however, when the PMS concentration exceeded this range, the performance of the CoCu10/PMS process declined with the increase in PMS concentration. One possible explanation for this trend is that at relatively high concentrations of PMS, the reactive sites of the catalyst became saturated, and the excess PMS in the system was unable to be effectively activated. Instead, excess PMS would react with newly generated ROS (i.e., self-quenching effect), thereby inhibiting the removal of pollutants in the system.

The influence of temperature on the CoCu10/PMS process was also investigated. As illustrated in Fig. S12a, the removal of TC significantly accelerated with the increase of temperature, implying that the reaction in the system is endothermic. As the reaction temperature increased from 15°C to 45°C , k_{obs} increased from 0.5765 min^{-1} to 1.1974 min^{-1} (Fig. S12b). Based on the available data, the activation energy (E_a) of the reaction was further determined using the Arrhenius equation, which was found to be 17.12 kJ/mol (Fig. S12c). This value exceeds the typical diffusion-limited reaction value (10–13 kJ/mol), indicating that the k_{obs} of the reaction process is predominantly governed by the rate of intrinsic chemical reaction on the CoCu10 surface, rather than the rate of mass transfer [40].

The stability of the CoCu10/PMS process in the removal of TC was evaluated by ten consecutive runs under identical conditions. As shown in Fig. 2c, the performance of the CoCu10/PMS process shows little reduction after eight cycles. The TC in the system was still removed by more than 97% within 10 min at the eighth cycle, which presents the unparalleled stability of the CoCu10/PMS process.

The influence of initial pH was shown in Fig. 2d. The process proved to be effective in TC removal over a wide pH range (pH 7–11), while acidic conditions were found to be unfavorable for the removal of TC. To provide an explanation for this observation, we examined the zeta potential of CoCu10 (the illustration in Fig. 2d) and the changes in pH during the reaction (Fig. S13). The pH_{zpc} of CoCu10 was calculated to be 7.30. Furthermore, we noted that the addition of PMS did not significantly alter the pH, possibly due to the buffering effect of surface hydroxyls of CoCu10 [41].

When the initial pH was 3 and 5, the solution was still acidic after adding PMS. In acidic medium, a large amount of H⁺ would bind to the peroxide of PMS and inhibit the interaction between PMS and CoCu10 [42]. Moreover, H⁺ could also stabilize the PMS, making it more challenging to activate [43]. Although the positively charged surface of CoCu10 in the acidic medium was favorable for its electrostatic adsorption to PMS, the undesirable effects due to H⁺ mentioned above would severely impede the activation of PMS. When the initial pH was 6.35–9, the pH of the reaction system could maintain a nearly neutral state after adding PMS. In this state, the adverse effects of H⁺ disappeared, and the surface of CoCu10 remained positively charged, ensuring adequate contact with PMS. All these factors jointly ensured the efficient removal of TC in neutral and weakly alkaline environments. When the initial pH was 11, the removal efficiency of TC by the CoCu10/PMS process decreased slightly. It could be found that the pH of the system dropped to approximately 10.65 after the addition of PMS. At this pH, PMS mainly existed in the form of SO₅²⁻, and TC mainly existed as TC²⁻ [44]. On the other hand, the surface of CoCu10 was highly

negatively charged, which means that there would be a strong electrostatic repulsion among PMS, TC and CoCu10. This electrostatic repulsion would impede the catalytic process. Additionally, it's possible that the strong alkaline environment caused the deprotonation of surface hydroxyls of the catalyst, thereby reducing the potential reactive sites and slightly inhibiting the activation process.

The leaching behavior of Co and Cu during the reaction was evaluated. As depicted in Fig. S14, the Co leaching concentration of CoCu10 was found to be only 4.01 µg/L, significantly lower than that of CoOOH (9.89 µg/L). Similarly, the leaching concentration of Cu in CoCu10 was observed to be 966.13 µg/L. Overall, the leaching of Co and Cu from CoCu10 during the reaction process was well below the permissible limit (Co < 10 µg/L, Cu < 1000 µg/L) specified in the Standards for Drinking Water Quality (GB 5749–2022), which indicate that CoCu10 would not pose a potential threat to the aquatic environment due to metal leaching.

3.3. Identification of ROS and active sites

3.3.1. Radical pathway

To gain insight into the activation mechanism of CoCu10 on PMS, quenching experiments were conducted. The radical pathway in the system was investigated initially. EtOH, known for its fast reaction rate with SO₄²⁻ ($k = 1.6 \times 10^9$ – $7.7 \times 10^9 \text{ M}^{-1}\text{s}^{-1}$) and •OH ($k = 1.2 \times 10^9$ – $2.8 \times 10^9 \text{ M}^{-1}\text{s}^{-1}$) [25], was often used as a scavenger for these radicals [45]. TBA was a more effective scavenger of •OH ($k = 3.8 \times 10^8$ – $7.6 \times 10^8 \text{ M}^{-1}\text{s}^{-1}$) [45]. Fig. 3a shows that low dose (10 mM) EtOH had little effect on the reaction system and even 100 mM EtOH had an insignificant effect on the removal of TC within 10 min. Moreover, increasing the concentration of EtOH did not enhance the inhibitory effect on the reaction system, as the inhibitory effect of 500 mM EtOH on TC removal was almost the same as that of 100 mM EtOH. The inhibition of TC removal by different concentrations of TBA was also insignificant, as shown in Fig. 3b. These results suggest that that •OH and SO₄²⁻ were not the main active species in the reaction. Additionally, p-nitrophenol (NB), with an electron-withdrawing nitro group, has a high ionization potential, which results in its oxidation occurring only by radical pathways rather than non-radical pathways [46]. As shown in Fig. S15, the CoCu10/PMS process exhibited almost no oxidation capability for NB, indicating that the CoCu10/PMS process was predominantly dominated by non-radical pathway with the selectivity.

The EPR results also confirmed that the contribution of the radical pathway to TC removal was small. 5,5-Dimethyl-1-pyrroline-N-oxide (DMPO) was used as a spin-trapping agent to explore SO₄²⁻ and •OH in the reaction system. As shown in Fig. 3e, no signals of DMPO-SO₄²⁻ and DMPO-•OH were observed from the beginning to the end, instead, the signals of 5,5-dimethyl-2-pyrrolidone-N-oxyl (DMPOX) with seven narrow peaks were observed. Some reports have confirmed that there are two reasons for the conversion of DMPO to DMPOX: i. Excessive oxidation by radicals (i.e., SO₄²⁻ and •OH). ii. Oxidation by some non-radical pathways. In order to identify the origin of DMPOX, MeOH was used to scavenge radicals in the reaction system. After adding MeOH, the signal of DMPOX still existed, which ruled out the over-oxidation by radicals and indicated the existence of non-radical pathways in the system.

In addition, chloroform (CF) was used to identify the presence of O₂^{•-} in the system [47]. As presented in Fig. 3c, the addition of 0–10 mM CF had only a very weak inhibition on the removal of TC in the reaction system. This result indicates that the contribution of O₂^{•-} to the removal of TC was minor, further emphasizing that the radical pathway didn't play a crucial role in the CoCu10/PMS system. The corresponding EPR spectrum also confirmed this, only extremely weak DMPO-O₂^{•-} signals were detected within 10 min, and the intensity did not change during the reaction, indicating that O₂^{•-} contributed less to the removal of TC in the system (Fig. 3f).

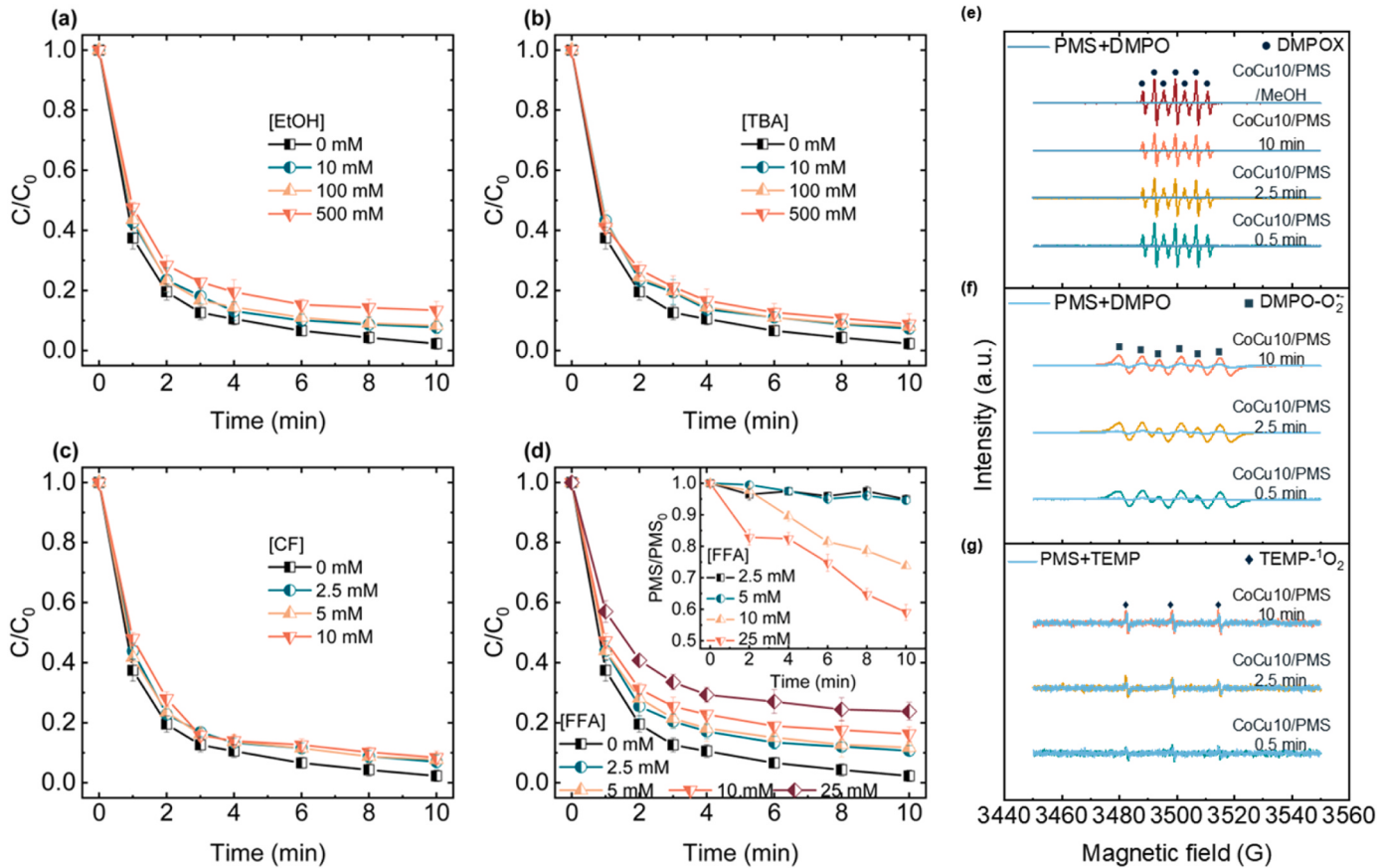


Fig. 3. Scavenging effect of (a) EtOH, (b) TBA, (c) CF and (d) FFA on the CoCu10/PMS system, and the illustration in (d) shows the consumption of PMS by FFA. EPR spectra for the detection of (e) DMPOX, (f) DMPO-O₂⁻ and (g) TEMP-¹O₂ in the presence of DMPO and TEMP. Reaction conditions: [TC] = 22.5 μ M, [Catalyst] = 0.20 g/L, [PMS] = 0.2 mM, [Temperature] = 25 °C and [initial pH] was unadjusted.

3.3.2. Singlet oxygen

Due to its extremely high reactivity with $^1\text{O}_2$, FFA was chosen as a scavenger for $^1\text{O}_2$ ($k = 1.2 \times 10^8 \text{ M}^{-1}\text{s}^{-1}$) [48]. As shown in Fig. 3d, the inhibition of TC removal was gradually enhanced with the increase of FFA concentration, which seems to imply that $^1\text{O}_2$ has a certain contribution to TC degradation. However, it has been confirmed that FFA and some other $^1\text{O}_2$ scavengers, such as L-histidine and NaN₃, could react directly with PMS, which may lead to false positive results. Given this, the consumption of PMS by FFA was monitored [49]. As shown in illustration of Fig. 3d, sole FFA could indeed directly react with PMS, and at a concentration of 25 mM FFA, it could even consume about 41% of PMS within 10 min. Therefore, quenching experiments seem to be unsuitable for identifying the contribution of $^1\text{O}_2$. As previously reported, EPR spectroscopy was used to identify $^1\text{O}_2$ in the system, and 2,2,6,6-tetramethylpiperidine (TEMP) was used as a spin trapping agent for $^1\text{O}_2$ [50]. As depicted in Fig. 3g, the sole PMS was capable of oxidizing TEMP, exhibiting a typical 2,2,6,6-tetramethyl-1-piperidinyloxy (TEMPO) signal with triple peaks. However, in the presence of CoCu10, the intensity of the TEMPO signals remains almost identical to that observed in the system containing only PMS, suggesting that even in the CoCu10/PMS system, the generation of the TEMPO signals was mainly due to the direct oxidation by PMS. Furthermore, the intensity of the TEMPO signals did not increase significantly over time, indicating that activation of PMS by CoCu10 hardly produced $^1\text{O}_2$. In addition, the degradation of TC in D₂O did not show a significant difference compared to that in water, which also indicates that there was almost no $^1\text{O}_2$ in the CoCu10/PMS system (Fig. S16) [51]. In summary, it could be concluded that the non-radical pathway of $^1\text{O}_2$ was almost negligible for the removal of TC in the system.

3.3.3. Catalyst-mediated electron transfer

The catalyst-mediated electron transfer is a unique non-radical pathway, in which the catalyst acts as a bridge for electron transfer, while the PMS and pollutant serve as electron donors and acceptors, respectively. For this pathway, PMS would only undergo decomposition when both PMS and pollutants are present in the reaction system. In other words, the decomposition rate of PMS in a reaction system containing pollutants would definitely be higher than that in a system without pollutants at the same time [52]. As shown in Fig. S17a in the above, the decomposition rate of PMS in the system containing TC was significantly lower than that in the system without TC, indicating the absence of catalytic electron transfer pathways in the reaction system. The existence of this pathway can also be judged by monitoring the change of the i-t curve after the addition of PMS and pollutants [53]. As shown in Fig. S18, a sharp increase in the current was observed after adding PMS, indicating the existence of rapid electron transfer between CoCu10 and PMS. However, after the addition of TC, the current did not change significantly, indicating that there was no electron transfer between TC and CoCu10, which directly denies the existence of catalyst-mediated electron transfer pathway. It is worth mentioning that the current change amplitude of CoOOH was much smaller than that of CoCu10, indicating that Cu doping could improve the electron transfer rate of the catalyst. In addition, the LSV curves show that the presence or absence of TC could not affect the current intensity in the presence of PMS, which also proves that the above pathway did not exist in the CoCu10/PMS system (Fig. S19). Finally, in order to most intuitively verify whether the electron transfer pathway existed in the system, a galvanic oxidation processes (GOP) system was constructed (Fig. S17b). If pollutants in the GOP system can be continuously degraded, it indicates the presence of the electron transfer pathway [52]. It could be

seen that the TC concentration in the GOP system decreased slightly within the first hour, which could be attributed to the adsorption of TC by the electrodes. During the subsequent 5 h, the TC concentration remained unchanged, which proved that CoCu10 could not mediate the electrons transfer from TC to PMS.

3.3.4. High-valent cobalt-oxo species

Given that the common activation pathways mentioned earlier are not applicable to the CoCu10/PMS system, we have to suspect the possible existence of high-valent metal-oxo species (HVMS) in this system. Dimethyl sulfoxide (DMSO) is used to scavenger HVMS due to its

high reaction rate with HVMS [14]. Fig. 4a illustrates that a low concentration of 20 mM DMSO could effectively inhibit the TC removal in the system, and the inhibition on TC removal increased with increasing concentration. At 100 mM, the inhibition was most significant, resulting in a decrease in TC removal from 97.7% to 37.0%. This result strongly implies that in the CoCu10/PMS system, HVMS is the dominant ROS.

To further confirm, an investigation was conducted using phenyl-methyl sulfoxide (PMSO) as a probe. It has been confirmed that PMSO could be selectively oxidized to phenylmethyl sulfone (PMSO₂) by high-valent metal-oxo species including Co(IV)=O, while other ROS and Cu (III) do not exhibit selectivity towards the oxidation of PMSO (Fig. 4b)

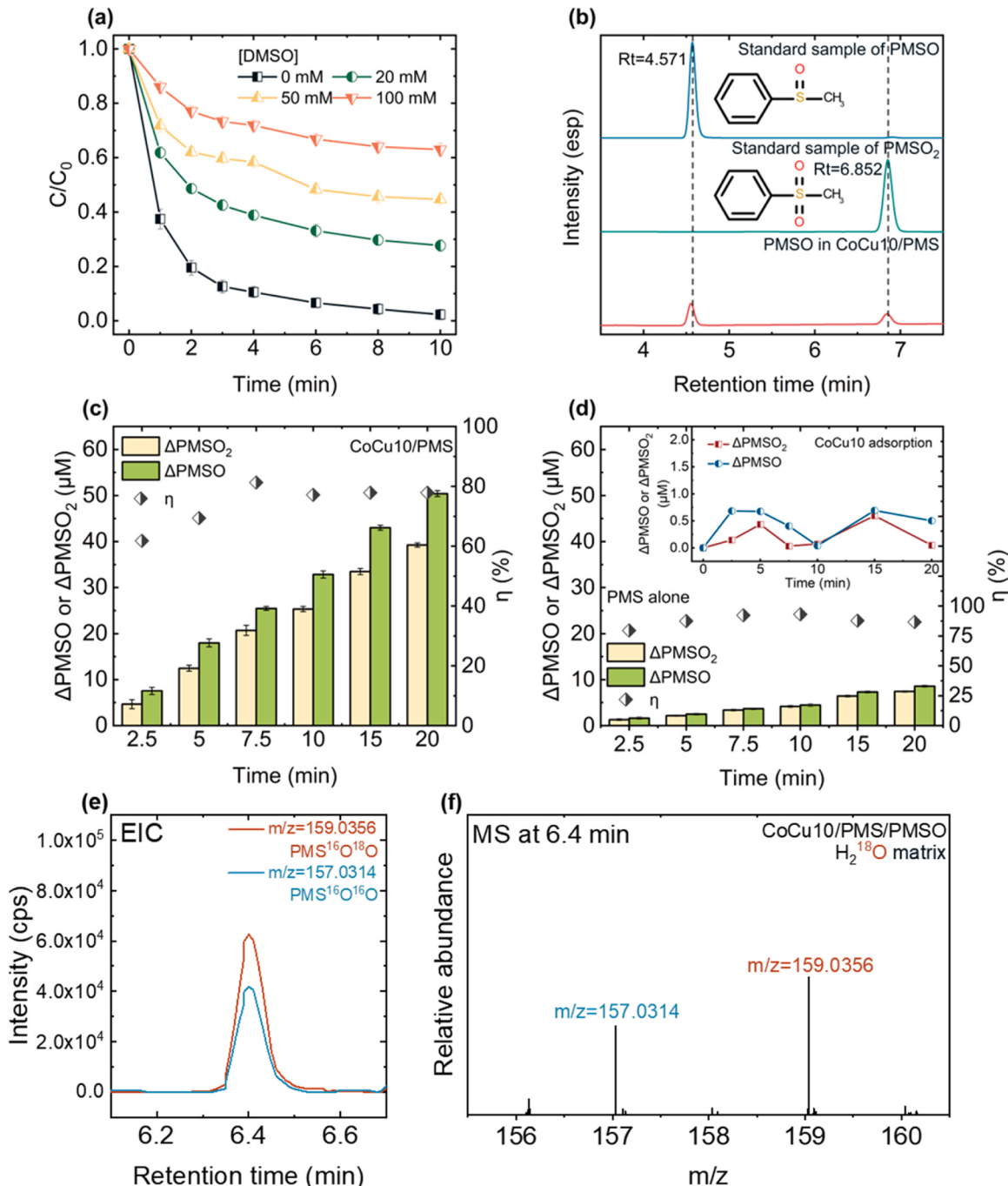


Fig. 4. (a) Scavenging effect of DMSO on the CoCu10/PMS system. (b) Chromatogram of pure PMSO, PMSO₂ and PMSO after degradation. Conversion of PMSO in CoCu10/PMS system (c) and sole PMS system (d), and the illustration in (d) shows the adsorption of PMSO by CoCu10 (e) extracted ion chromatogram (EIC) of PMS¹⁶O¹⁸O ($m/z = 156.0356$ [$\text{M}+\text{H}^+$]) and PMS¹⁶O¹⁸O ($m/z = 159.0356$ [$\text{M}+\text{H}^+$]); and (f) MS spectrum of PMS¹⁶O¹⁶O/PMS¹⁶O¹⁸O in the CoCu10/PMS system. Reaction conditions: [PMSO]= 200 μM , [Catalyst]= 0.20 g/L, [PMS]= 0.2 mM, [Temperature]= 25 °C and [initial pH] was unadjusted.

[14,54]. Hence, by monitoring the consumption of PMSO (ΔPMSO) and the generation of PMSO_2 (ΔPMSO_2) during the reaction process, it is possible to judge whether the HVMS is Co(IV) or Cu(III), and roughly estimate the corresponding contribution. Fig. 4c illustrates the transformation of PMSO in different systems. Within 20 min, a total of 50.42 μM of PMSO was oxidized, while 39.27 μM of PMSO_2 was produced during the same time period, resulting in an overall conversion rate (η , $\eta = \Delta\text{PMSO}_2/\Delta\text{PMSO}$) of around 80%. PMS also oxidizes PMSO

to PMSO_2 , as shown in Fig. 4d, where 8.57 μM of PMSO was oxidized and 7.43 μM of PMSO_2 was produced within 20 min. In addition, it was observed that the concentrations of PMSO and PMSO_2 remained almost unchanged in the presence of sole CoCu10, indicating that the adsorption/oxidation effect of CoCu10 alone can be ignored (illustration in Fig. 4d). Using this result to correct ΔPMSO or ΔPMSO_2 in the CoCu10/PMS system, the overall η was found to be around 75%, proving that Co(IV) was the dominant ROS in the CoCu10/PMS system.

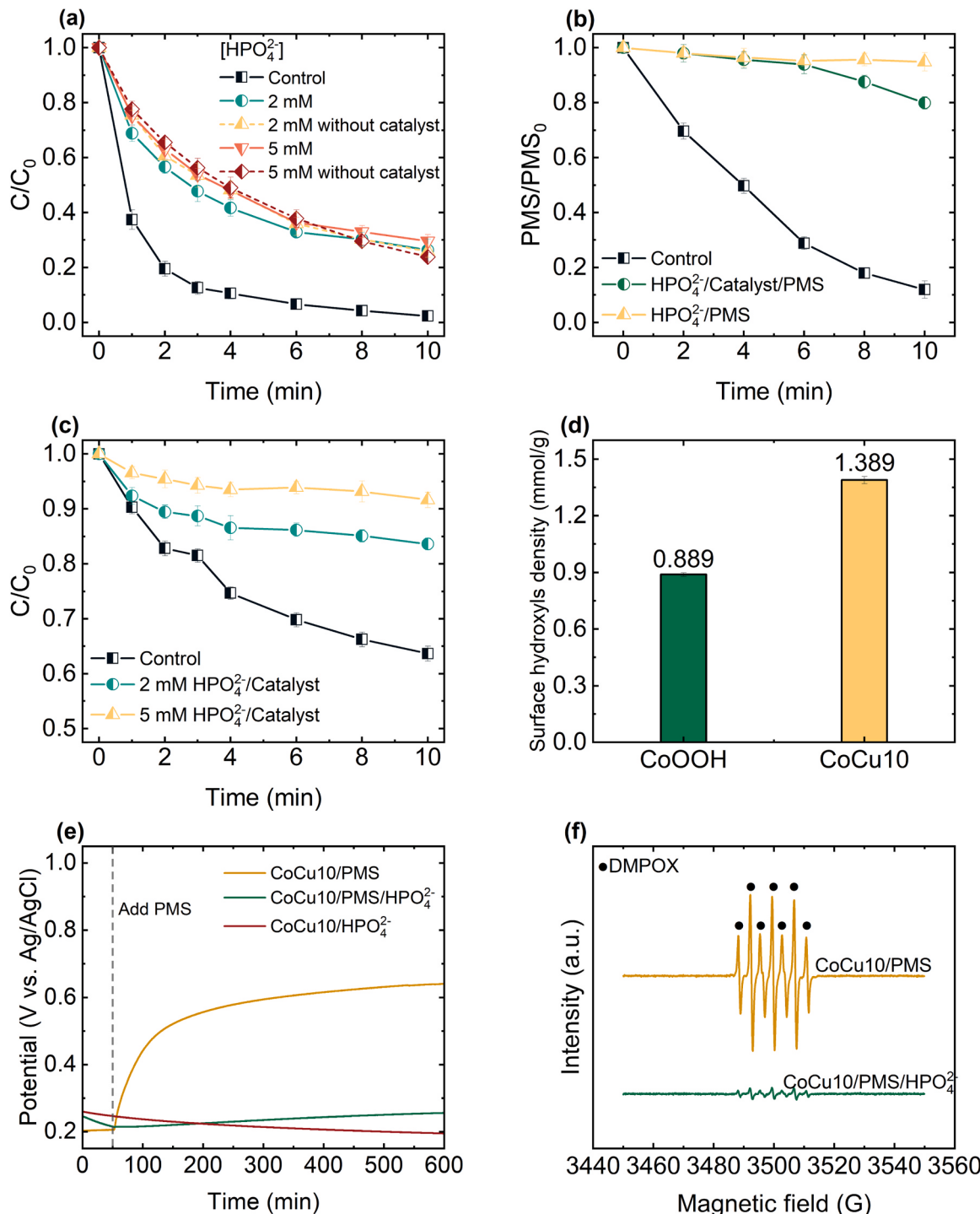


Fig. 5. Effect of phosphates on (a) TC degradation and (b) PMS decomposition in CoCu10/PMS system. (c) Effect of phosphate on the adsorption of TC by the catalyst. (d) The surface hydroxyl density of CoOOH and CoCu10. (e) Open circuit potential of CoCu10 in different systems. (f) EPR spectra of the CoCu10/PMS system in the presence or absence of phosphate with DMPO as the spin trapping agent. Reaction conditions: [TC] = 22.5 μM , [Catalyst] = 0.20 g/L, [PMS] = 0.2 mM, [Temperature] = 25 °C and [initial pH] was unadjusted.

Due to the capability of Co(IV)=O to undergo oxygen atom exchange (OAE) with H₂O, the ¹⁸O isotope-labeled experiment is considered the golden standard for identifying the presence of Co(IV)=O [55]. Therefore, H₂¹⁸O was utilized as the matrix to investigate the transformation of PMSO in the CoCu10/PMS system. In the ESI positive mode, two peaks with identical retention times (Rt=6.40 min) were observed in the EIC (Fig. 4e), with *m/z* values of 157.0314 and 159.0356 for the two substances (Fig. 4f), which can be assigned to PMS¹⁶O¹⁶O and PMS¹⁶O¹⁸O. The formation of PMS¹⁶O¹⁸O validates the formation of the Co(IV)=O species. Furthermore, numerous reports have confirmed that the sole PMS only can transform PMSO to PMS¹⁶O¹⁶O and cannot lead to the formation of PMS¹⁶O¹⁸O [14,55]. Therefore, the detection of PMS¹⁶O¹⁸O can be directly attributed to the generation of Co(IV)=O in the CoCu10/PMS system. Furthermore, the CV curve also confirmed the presence of Co(IV)=O, as shown in Fig. S20. In the three-electrode electrochemical system containing PMS, a distinct peak appeared around 1.5 V, which can be attributed to the Co(III)/Co(IV) oxidation process, while the peak near 1.1 V can be assigned to the Co(II)/Co(III) oxidation process[56,57]. In conclusion, the combination of PMSO probe experiments, ¹⁸O-isotope- labeling experiments, and CV curves confirmed the formation of Co(IV)=O species in the CoCu10/PMS system.

3.3.5. Active sites

It has been established that the surface hydroxyls of many transition metal oxides are commonly utilized as active or adsorption sites for various catalytic processes, and this holds true for PMS activation as well [58,59]. HPO₄²⁻ has a strong affinity for surface hydroxyls, which can poison the sites by forming a complex with the surface hydroxyls [33]. As shown in Fig. 5a, sole HPO₄²⁻ has a certain activation ability for PMS, and this phenomenon has also been confirmed by many reports [60]. Notably, in the system with CoCu10, the removal trend of TC was almost identical to that in the HPO₄²⁻/PMS system, indicating that the activation of PMS by HPO₄²⁻ was the sole reason of TC degradation. The measured pH of the reaction system consistently remained within the range of 7.75–8.40 regardless of 2 mM or 5 mM HPO₄²⁻, which could rule out the adverse effect of changes in pH on reaction process. The decomposition of PMS in the presence of HPO₄²⁻ was also measured. As shown in Fig. 5b, the addition of HPO₄²⁻ almost entirely inhibited PMS decomposition by CoCu10, and the decomposition rate was greatly reduced from 88.1% to 20.0%, which indicates that CoCu10 has been almost completely inactivated in the presence of HPO₄²⁻. In addition, NaClO₄ hardly posed any inhibition to the reaction system (Fig. S21), indicating that the interaction between CoCu10 and PMS occurred through surface hydroxyls-mediated inner-sphere complexation rather than electrostatic adsorption. Altogether, these results provide strong evidences that surface hydroxyls are the active sites for CoCu10 to activate PMS. On the other hand, CoCu10 appeared to also serve as adsorption sites for TC. As shown in Fig. 5c, HPO₄²⁻ in the system can notably inhibit the adsorption of TC by CoCu10, and the inhibition increased with the concentration of HPO₄²⁻. PMS decomposition was also monitored in the system with or without TC (Fig. S17a). Interestingly, the presence of TC significantly reduced the decomposition rate, which was due to the fact that TC occupied part of activation sites of PMS. In addition, PMS was added to the system under the condition of CoCu10 pre-adsorbed TC, and the degradation of TC was significantly lower than that under normal conditions(Fig. S22). These results above prove the fact that both TC and PMS use the surface hydroxyls as the shared sites. Given the importance of surface hydroxyls in the activation/adsorption process, it is reasonable to hypothesize that one of the reasons for the difference in activation performance between CoCu10 and CoOOH is the difference in the density of surface hydroxyls. To further confirm the impact of Cu doping on the density of surface hydroxyls of CoOOH, two samples were subjected to saturated deprotonation experiments to accurately quantify their surface hydroxyl densities. As depicted in Fig. 5d, the result demonstrates that the surface

hydroxyl density of CoCu10 was 1.389 mmol/g, while that of CoOOH was only 0.889 mmol/g. Therefore, the activation performance of CoCu10 for PMS was also improved accordingly due to the increase of surface hydroxyl density.

Further investigation was conducted to help understand how surface hydroxyls influence the generation of Co(IV)=O. According to reports, HVMS is proposed to be generated through heterolytic cleavage of the O–O bond in the catalyst-PMS complex [56]. Therefore, the prerequisite for the formation of HVMS including Co(IV)=O is the coordination of metal sites with PMS to form catalyst-PMS complexes, which is crucial for the generation of HVMS. Given the significant influence of surface hydroxyls on the reaction, it is reasonable to speculate that these groups act as the bridge for the formation of PMS complexes, which can be proved by chronoamperometry. As depicted in Fig. 5e, upon PMS addition, the open-circuit potential of the CoCu10 electrode rapidly increased, reaching an equilibrium potential (i.e., the potential of PMS complexes) over time, which has been proved to be a sign of the formation of catalyst-PMS complexes [22]. Interestingly, in the presence of HPO₄²⁻, the potential increase induced by the addition of PMS was greatly inhibited. This is attributed to the surface hydroxyls of CoCu10 being occupied by phosphate, preventing the formation of PMS complexes due to their inability to coordinate with PMS. To further verify the importance of surface hydroxyls for Co(IV)=O formation, PMSO transformation experiments were conducted in the presence of HPO₄²⁻, as illustrated in Fig. S23a. Under the presence of HPO₄²⁻, both the CoCu10/PMS system and the PMS system exhibited almost identical consumption of PMSO and generation of PMSO₂ during the experimental process, which indicates that CoCu10 cannot continue to activate PMS to generate Co(IV)=O after HPO₄²⁻ occupied the surface hydroxyls. EPR also provided evidence to support this finding, as shown in Fig. 5f. After the addition of HPO₄²⁻ to the system, the signal intensity of DMPOX exhibited a significant reduction compared to the control, indicating that Co(IV)=O originated from the cleavage of the PMS complexes. The CV curve also offers direct evidence of the correlation between Co(IV)=O and surface hydroxyls (Fig. S23b). As mentioned earlier, the peaks around 1.5 V and 1.1 V in the CV curve of CoCu10 can be attributed to the Co(III)/Co(IV) and Co(II)/Co(III) oxidation process. However, these peaks disappeared in the solution containing HPO₄²⁻, directly demonstrating the strong dependency of Co(IV)=O generation process on surface hydroxyls. Combining the above results, during the process of PMS activation, surface hydroxyls acted as the coordination sites for PMS and were responsible for capturing PMS, forming PMS complexes. After the formation of PMS complexes, Co species in CoCu10 donated electrons to the PMS complexes, which led to the heterolytic cleavage of the O–O bond of the PMS complexes, and finally formed Co(IV)=O.

3.3.6. Homogeneous reaction in the system

On the flip side, leached metal ions may also have an activation effect on PMS. As shown in Fig. 6a, the leaching level of Co has almost no activation effect on PMS, and its degradation effect on TC was almost the same as that of sole PMS. However, the leached of Cu exhibited a certain activation performance, and TC in the corresponding homogeneous system could be degraded by 38.5% within 10 min, which indicates that there was a homogeneous pathway in the reaction system. To elaborate on this point, further exploration was conducted using EPR. Similarly, DMPO was employed as the spin trapping agent, but only the separated filtrate was analyzed, in contrast to the previous procedure. Interestingly, the filtrate did not show the signal of DMPOX as before. Instead, signals of DMPO-SO₄²⁻ and DMPO-•OH were detected at all three time points (Fig. 6b), indicating Cu²⁺ in the system could activate PMS by radical pathway. In addition, a series of TC removal experiments were conducted in the solution containing phenol. In fact, phenol tends to accumulate on the surface of the catalyst during the reaction due to its hydrophobicity, thus separating the surface of the catalyst from the medium, which can help to distinguish the contribution of homogeneous/heterogeneous reactions[61]. As shown in Fig. S24, 10 mM

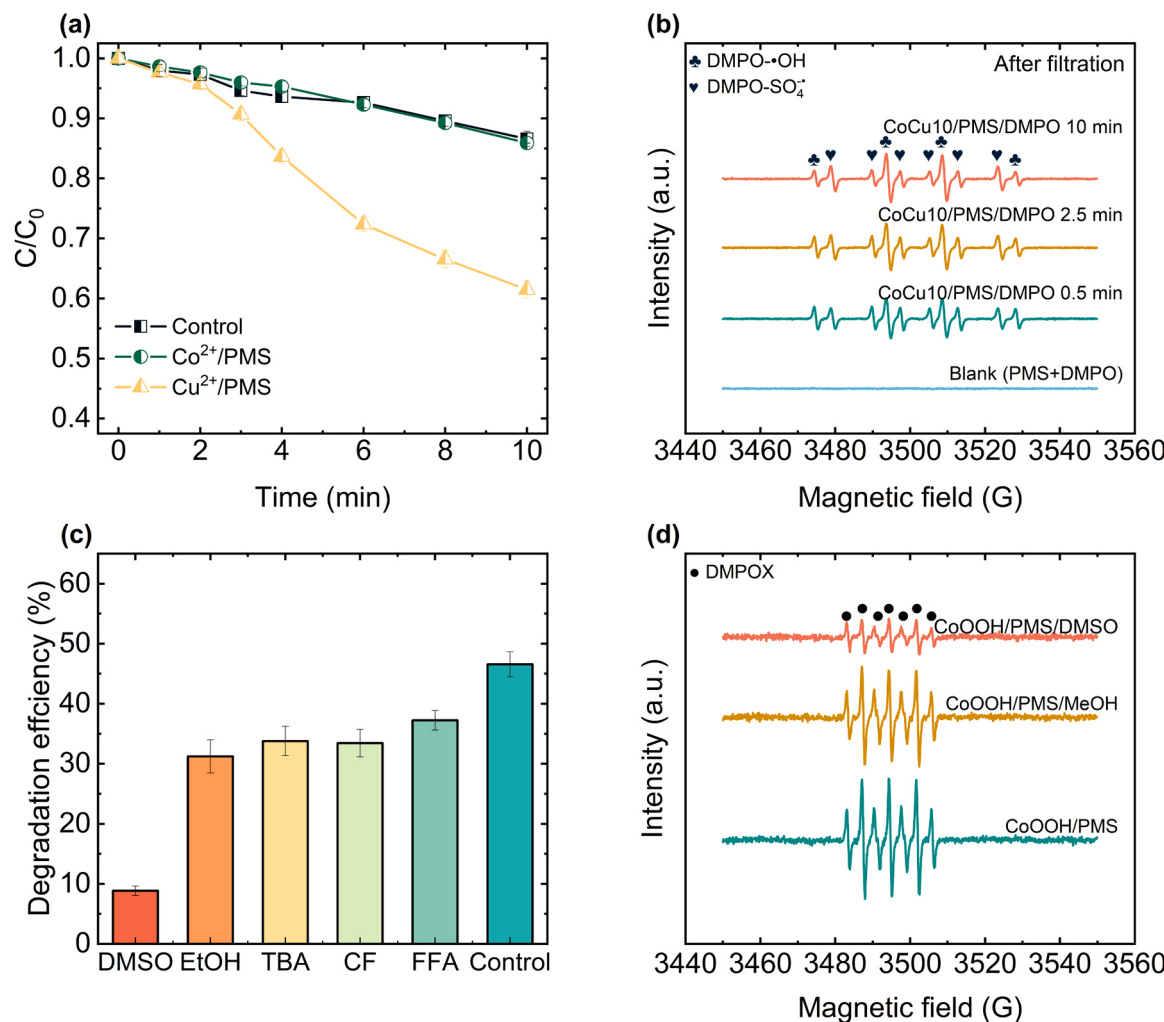


Fig. 6. (a) Activation performance of PMS at leaching levels of metal ions. (b) EPR spectra of the filtered supernatant of the CoCu10/PMS system (DMPO as spin trapping agent). (c) The scavenging effect of various quenchers on CoOOH. (d) The inhibition of methanol and DMSO on the DMPOX signals from the CoOOH/PMS system. Reaction conditions: [TC] = 22.5 μM , [Catalyst] = 0.20 g/L, [PMS] = 0.2 mM, [Temperature] = 25 °C, [Initial pH] was unadjusted, [DMSO] = 100 mM, [EtOH] = 500 mM, [TBA] = 500 mM, [CF] = 10 mM and [FFA] = 5 mM.

phenol could significantly inhibit the performance of the reaction system, and as the concentration of phenol increased, the TC removal in the system continued to decrease, implying that degradation of pollutants mainly depends on the heterogeneous reaction originating from Co(IV)=O rather than the homogeneous reaction originating from Cu ions.

3.3.7. The role of Cu

Besides increasing the surface hydroxyl density, the role of Cu needs to be further investigated. Quenching experiments were conducted on CoOOH to determine whether Cu doping altered the activation pathway for PMS. As shown in Fig. 6c, among several scavengers, DMSO had the most powerful inhibition on the reaction system, almost completely stopping the TC degradation, indicating that Co(IV) was likely the primary ROS in the CoOOH/PMS system. However, previous reports have suggested that pollutants in the CoOOH/PMS system were degraded through the radical pathway (i.e., $\text{SO}_4^{\cdot-}$ and $\bullet\text{OH}$), which appears to contradict our findings[24,62]. To clarify this point, the PMSO probe degradation experiment was conducted again. As shown in Fig. S25, within 60 min, 77.9 μM of PMSO was consumed, and 76.0 μM of PMSO_2 was generated in the CoOOH/PMS system. However, due to the relatively poor activation performance of CoOOH for PMS, most of the ΔPMSO and ΔPMSO_2 could be attributed to the oxidation by PMS alone. After subtracting the contribution of PMS, it was found that PMS could

be activated by CoOOH to oxidize 18.4 μM of PMSO, generating about 17.8 μM of PMSO_2 , with a conversion rate as high as 96.7%. This suggests that CoOOH primarily produced Co(IV) rather than other ROSs when activating PMS. This is further confirmed by EPR, as shown in Fig. 6d, where DMPO is oxidized to DMPOX instead of $\text{DMPO-SO}_4^{\cdot-}$ and $\text{DMPO}\bullet\text{OH}$ in the system. The introduction of methanol did not change the intensity of the DMPOX signal, which ruled out excessive oxidation by radical species[63]. The introduction of DMSO greatly suppressed the intensity of the signal, indicating that the signal of DMPOX originated from the direct oxidation of DMPO by Co(IV)=O [46]. Therefore, the introduction of Cu does not seem to change the dominant reaction pathway of the catalyst for PMS activation, and Co(IV)=O can be confirmed as the dominant ROS in the CoOOH/PMS system.

As established in the preceding sections, the Cu doping can significantly enhance the density of active sites (i.e., surface hydroxyls). In addition to this, it is necessary to investigate the influence of Cu doping on the thermodynamic aspects of activation process. The reaction free energies of activation of PMS by CoOOH and CoCu10 were calculated using DFT calculations to illustrate the positive effect of Cu introduction (Fig. S26). First, the surface hydroxyls on CoOOH and CoCu10 interacted with PMS to adsorb HSO_5^- onto the surface through an energy-releasing process with calculated potential barriers of -4.42 eV and -4.37 eV , respectively. Subsequently, PMS underwent proton transfer

on the surface of the two catalysts, leading to the formation of Co(IV)=O, and the energy barriers of this process were – 8.25 eV (CoOOH) and – 9.16 eV (CoCu10). Through the above calculations, the reaction energy barrier (–4.79 eV) of CoCu10 activated PMS is much lower than that of CoOOH (–3.83 eV), which shows the positive effect brought by the introduction of Cu.

3.4. Reaction mechanism

Techniques such as XRD, Raman, FTIR, SEM and XPS were employed to characterize CoCu10 before and after the reaction for a better understanding of the reaction mechanism. As shown in Fig. 7a, the catalyst

before and after the reaction was characterized using XRD, which revealed a continuously decrease in the crystallinity of CoCu10 as the reaction proceeded, indicating that the crystal structure of CoCu10 was damaged during the reaction. Interestingly, the results of the stability experiment mentioned earlier revealed that the activation performance of CoCu10 on PMS did not decrease within eight cycles. However, the crystal structure of CoCu10 was severely damaged during the first use, indicating that the activation of PMS by CoCu10 was non-crystal facet dependent. Raman spectra and SEM images also confirmed that the crystal structure of CoCu10 was damaged. After the reaction, the intensity of most characteristic peaks, except for the one at 676 cm⁻¹, decreased significantly (Fig. 7b). It is noteworthy that the peak at

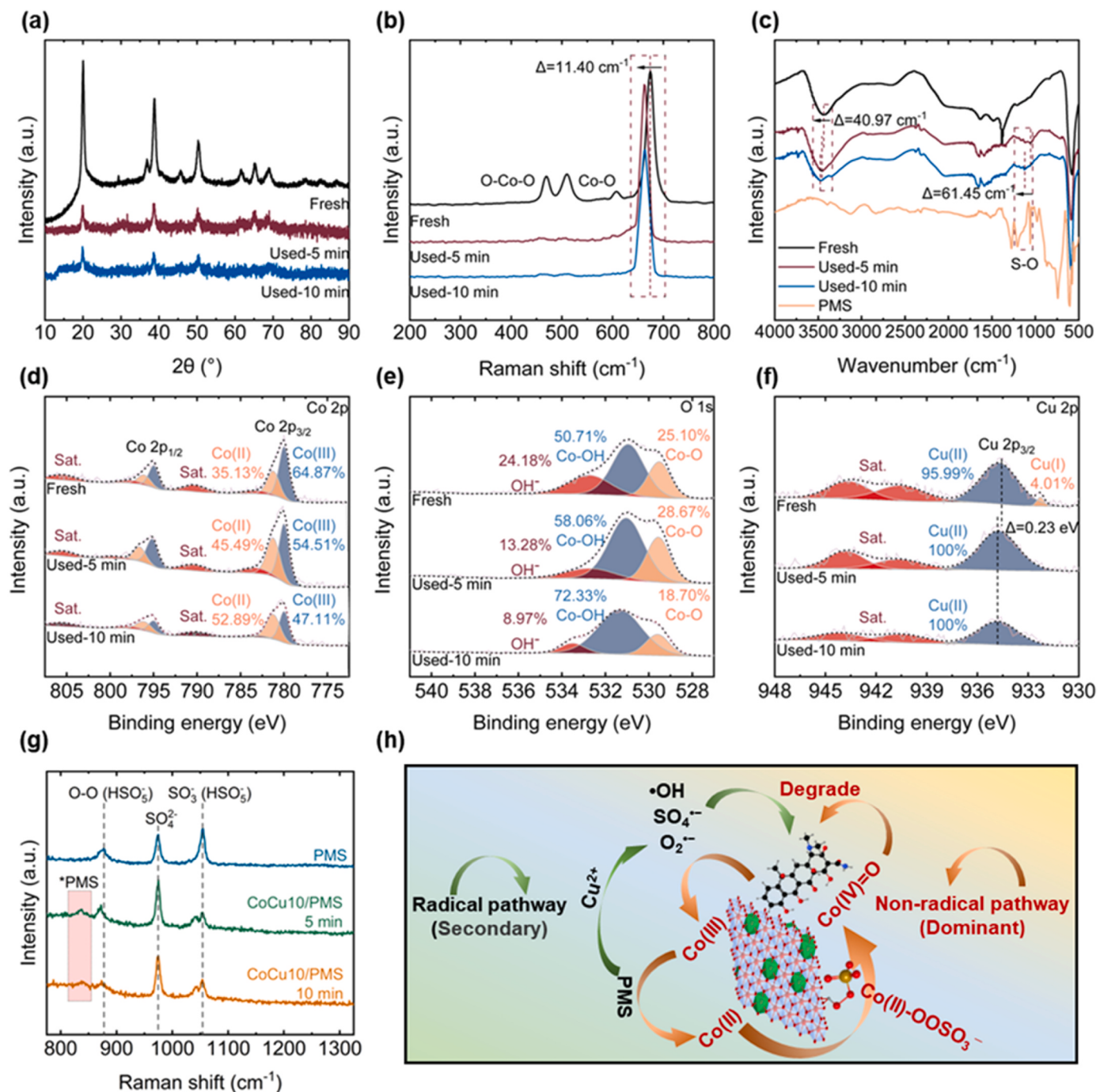


Fig. 7. (a)XRD, (b) Raman, (c) FTIR, and (d, e, f) XPS deconvolution spectra of CoCu10 before and after the reaction. (g) In-situ Raman spectra of the CoCu10/PMS system during the reaction process. (h) The reaction mechanism of CoCu10/PMS system.

676 cm⁻¹, which represents the symmetric vibration of O–H, not only did not show a significant decrease in intensity, but also experienced a red shift of approximately 11.4 cm⁻¹, indicating an increase in the length of the O–H bond, possibly due to the combination of HSO₅⁻ with surface hydroxyls. The SEM images reveal a significant transformation in the morphology of CoCu10 after use, and it shifted from a particle-like structure to a hollow, onion ring-like structure (Fig. S27). This transformation suggests that the crystal structure of CoCu10 has been greatly disrupted, which confirmed again that the activation of PMS by CoCu10 may not be dependent on specific crystal facet. Furthermore, the EDS mapping (Fig. S28) show that sulfur was also evenly distributed on the surface of the used CoCu10, which could be attributed to the adsorption of HSO₅⁻ on the surface of catalysts.

FTIR was used to investigate the changes in surface chemical bond states before and after the reaction. As shown in Fig. 7c, two new sets of peaks were observed in the used sample, including a broad band from 1015.8 to 1254.5 cm⁻¹ and a characteristic peak at 2321.8 cm⁻¹. These new peaks were also observed in the spectrum of PMS, with the one at 2321.8 cm⁻¹ could attribute to the antisymmetric stretching vibration of CO₂ in the atmosphere, while the broad band from 1015.8 to 1254.5 cm⁻¹ could be assigned to the stretching vibration of S–O bonds in HSO₅⁻, which is considered a key fingerprint of PMS[64]. Therefore, the presence of this band in the spectrum of the used CoCu10 could be considered direct evidence of the adsorption of HSO₅⁻ onto the catalyst surface. Furthermore, it is noteworthy that as the reaction progressed, the aforementioned band continually shifted towards higher wavenumbers. This phenomenon could be attributed to the interaction between the catalyst and PMS, resulting in a change in the electron density of PMS. This shift was also widely regarded as crucial evidence for the formation of an inner-sphere complex of HSO₅⁻ on the catalyst surface [64,65].

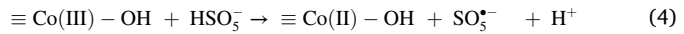
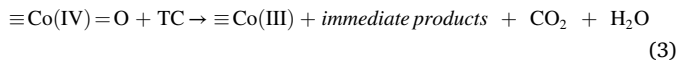
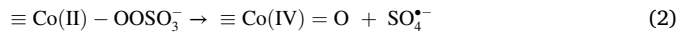
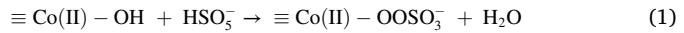
In addition, XPS was used to characterize the fresh and used samples. Comparing the Co 2p spectra of several samples, it was found that the proportion of Co(II) decreased continuously with the progress of the reaction, while the proportion of Co(III) increased (Fig. 7d). This phenomenon is reasonable, as Co(II) could be converted to Co(IV)=O via a two-electron pathway under the action of PMS, and then Co(IV)=O could be reduced to Co(III) after reacting with pollutants[15]. Fig. 7e displays the O 1 s spectrum of samples with different reaction times, which demonstrates a continuous decrease in the proportion of surface hydroxyls with the progress of the reaction, providing further evidence that surface hydroxyls serve as the active sites for CoCu10 in activating PMS. The changes of Cu species during the reaction were also studied, and interestingly, the valence of Cu did not appear to change throughout the reaction (Fig. 7 f). After 5 min of the reaction, it was observed that the original trace amount of Cu(I) was completely converted to Cu(II), which may be attributed to the direct oxidation of Cu(I) by PMS. Furthermore, the shift of 0.23 eV towards a higher binding energy region in the Cu 2p_{3/2} peak of the used, compared to the fresh sample, also suggests the conversion of Cu(I) to Cu(II). After 10 min of reaction, the binding energy of the Cu 2p_{3/2} peak was the same as that after 5 min, indicating that Cu(II) did not convert to another valence of Cu. This result is very intriguing, as previous reports have suggested that doped metals typically serve as promoters for redox cycling of the main metal in SR-AOPs systems[66,67]. But in this work, the doped Cu appears to not directly participate in the reaction but instead indirectly participates in the reaction by regulating the physicochemical properties of CoOOH.

The in-situ Raman spectrum was employed for a more detailed examination of the interaction between CoCu10 and PMS in the activation process (Fig. 7 g). The peaks at 877 cm⁻¹ and 1054 cm⁻¹ correspond to the O–O bond and SO₃⁻ in HSO₅⁻, while the peak at 975 cm⁻¹ is linked to the symmetric stretching vibrational mode of the S=O bond in SO₄²⁻[68]. Notably, in the CoCu10/PMS system, a peak absent in the PMS solution emerged at 836 cm⁻¹. This peak can be attributed to the formation of peroxy-species bound on the catalyst surface (i.e., catalyst-PMS complexes), confirming again the formation of PMS

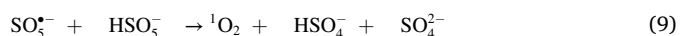
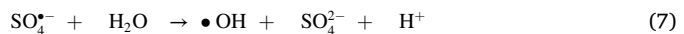
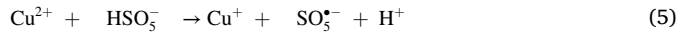
complexes on the surface of CoCu10[56]. Furthermore, a slight splitting of the SO₃⁻ peak in the low wavenumber direction indicates a redshift of this peak (shifting from 1054 cm⁻¹ to 1048 cm⁻¹). Simultaneously, the peak corresponding to the O–O bond also experienced a redshift of approximately 5 cm⁻¹ (shifting from 877 cm⁻¹ to 872 cm⁻¹). Redshift typically signifies an increase in electron density, suggesting that CoCu10 continuously donated electrons to PMS[37]. This electron-donating process led to the oxidation of Co species on the catalyst surface to form Co(IV)=O, while the PMS was reduced at the same time. Finally, it is also observable that in comparison to PMS, the intensity of peaks in the CoCu10/PMS system have changed. For example, an increase was observed in the peak of SO₄²⁻, while a decrease was observed in SO₃⁻ peak. This phenomenon arises from the rapid activation of PMS by CoCu10, leading to the rapid consumption of PMS and the concurrent accumulation of SO₄²⁻.

Based on the above discussion, a reasonable mechanism was proposed to describe the process of CoCu10 activating PMS to degrade TC (As shown in Fig. 7 h). Among Co(III) and Co(II) species, PMS prefer to interact with Co(II) to form Co(IV)=O via a two-electron transfer pathway, which was also confirmed by the continuous decrease of the Co (II) proportion in the Co 2p spectrum of CoCu10 before and after the reaction (Fig. 7d)[15]. So, the Co(II) sites in CoCu10 initially coordinate with the O atom from HSO₅⁻ through surface hydroxyls, forming the Co (II)–OOSO₃⁻ complexes (Eq. 1). The main ROS, ≡Co(IV)=O, was generated through heterolytic cleavage of the O–O bond in the Co(II)–OOSO₃⁻ complexes (Eq. 2). In this process, a small amount of SO₄²⁻ was unavoidably released[9]. But its contribution to the degradation of pollutants has been confirmed to be minimal. Then, Co(IV)=O directly attacked the TC adsorbed on the catalyst surface, leading to the degradation of TC, while Co(IV) was reduced to Co(III) via a one-electron pathway (Eq. 3). It has been well-established that Co(III) can accept electrons from PMS[24]. Therefore, Co(III) was reduced to Co(II) after accepting electrons donated by PMS, finally completing a cycle. (Eq. 4). In addition to the above pathways, there were also a small portion of radical pathways in the system, namely the activation of PMS by leached Cu ions, which generated a small amount of SO₄²⁻•OH, ¹O₂ and O₂^{•-} to degrade TC during this process (Eqs. 5–10)[69,70].

Dominant pathway:



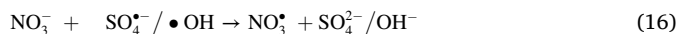
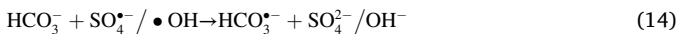
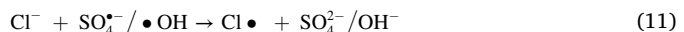
Secondary pathway:



3.5. Performance in different saline environments and real waters

Inorganic anions are present in most actual wastewater and have detrimental impacts on radical-based AOPs, but not significant effects on non-radical AOPs. To demonstrate this, five common anions, including

Cl^- , HCO_3^- , NO_3^- , SO_4^{2-} and H_2PO_4^- , were added at different concentrations to the CoCu10/PMS system as a proof of concept. Fig. 8a demonstrates that 2–250 mM Cl^- had almost no effect on TC removal. In SR-AOPs based on radicals, Cl^- could combine with SO_4^{2-} or $\bullet\text{OH}$ to produce secondary chlorine radicals (i.e., $\text{Cl}\bullet$, $\text{Cl}_2^{\bullet-}$, and $\text{ClOH}^{\bullet-}$) with lower oxidation potential (Eqs. 11–13), causing inhibition of pollutant removal in the reaction system[71]. This inhibitory effect was absent in the CoCu10/PMS system, which supports the dominance of Co(IV)=O in real wastewater. Similar to Cl^- , HCO_3^- could act as effective scavengers of radicals, reacting with SO_4^{2-} or $\bullet\text{OH}$ to generate HCO_3^- or CO_3^{2-} with lower oxidation potential (Eqs. 14 and 15)[72]. In the CoCu10/PMS system, the TC removal was almost unaffected by the presence of 0–250 mM HCO_3^- , which presents the unparalleled selectivity of Co(IV) (Fig. 8b). Furthermore, NO_3^- could also react with SO_4^{2-} or $\bullet\text{OH}$, forming NO_3^\bullet (Eq. 16), which effectively scavenges radical species in the system, but leaving the non-radical pathways unaffected[73]. Obviously, in the concentration range of 0–250 mM, no inhibition of NO_3^- on the system was observed (Fig. 8c).



Unlike the aforementioned anions, SO_4^{2-} appeared to pose a weak inhibitory effect for the reaction system (Fig. 8d). According to reports, SO_4^{2-} cannot react with radical species to generate secondary radicals, so its weak inhibition on the reaction system was not attributed to the scavenging effect of the anion. In fact, the scavenging effect of anions is

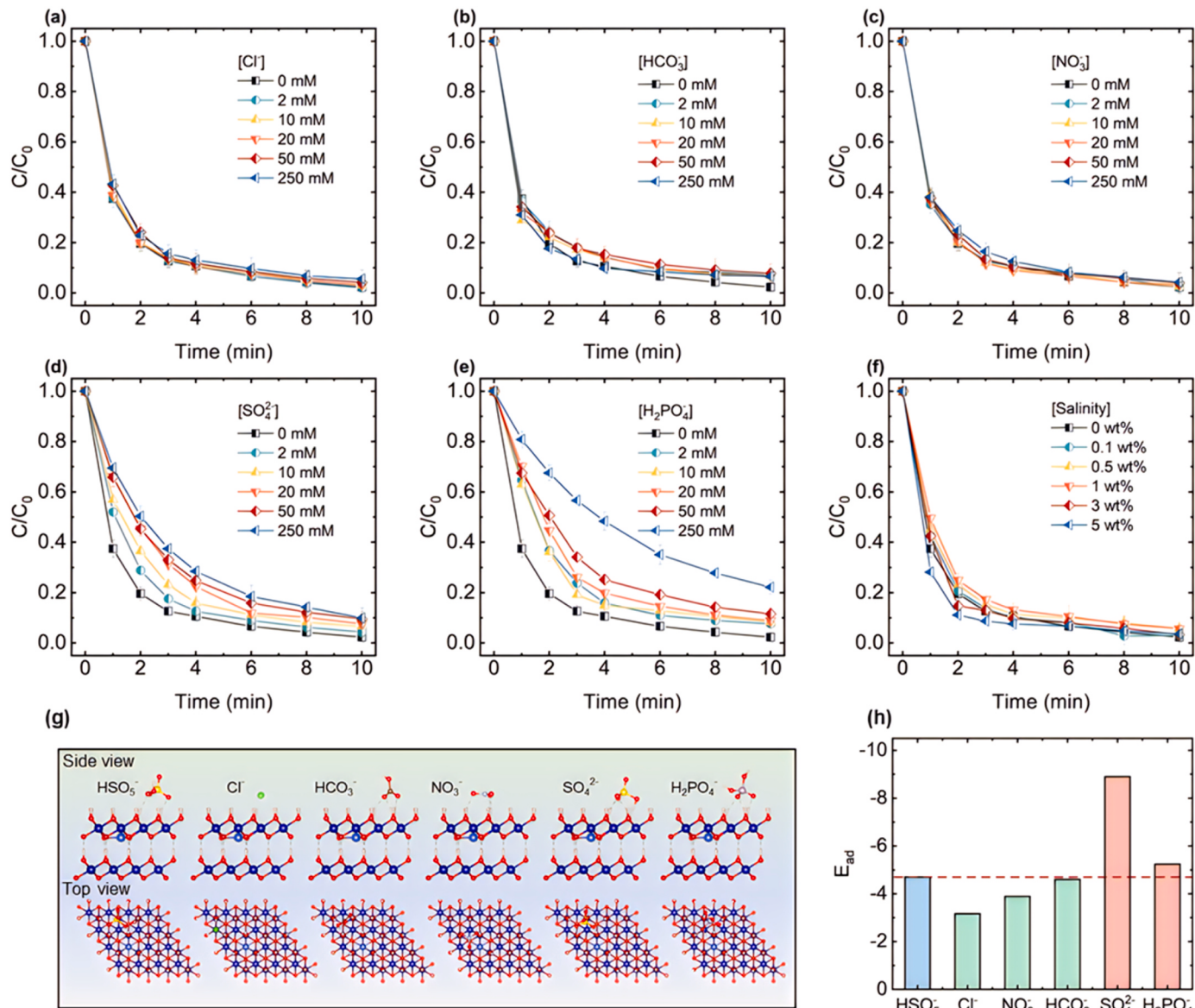


Fig. 8. Removal of TC under different concentrations of (a) Cl^- , (b) HCO_3^- , (c) NO_3^- , (d) SO_4^{2-} and (e) H_2PO_4^- . (f) Removal of TC in CoCu10/PMS system at different salinity. (g) Adsorption configurations of different anions on CoCu10. (h) Adsorption energies of CoCu10 for different anions. Reaction conditions: [TC]= 22.5 μM , [Catalyst]= 0.20 g/L, [PMS]= 0.2 mM, [Temperature]= 25 °C and [initial pH] was unadjusted.

not the only reason for inhibition, the competition for active sites of the catalyst can also lead to a decrease in the performance of the reaction system[74]. It has been confirmed that the surface hydroxyls of transition metal oxides are the adsorption sites of sulfates. Therefore, in the reaction system, SO_4^{2-} could compete with PMS for the surface hydroxyls of CoCu10, leading to a decrease in the performance. But overall, this inhibition did not pose a significant impact for TC removal. Under high concentration of 50 mM SO_4^{2-} , the TC removal in the reaction system could still reach more than 93%, and even under ultra-high concentration of 250 mM, about 90% of TC was still rapidly removed within 10 min. The inhibition of H_2PO_4^- on the system could also be attributed to the competition for active sites. In addition, H_2PO_4^- itself also dissociated in water to release a small amount of HPO_4^{2-} (Eq. 17), which could quickly complex with the surface hydroxyls of CoCu10, thus occupying the active sites[33]. From Fig. 8e, it can be seen that the inhibition of TC removal by H_2PO_4^- in the range of 0–50 mM was weak, and TC removal in the system was always around 90% or higher. The performance of CoCu10/PMS was indeed significantly affected by 250 mM H_2PO_4^- , but about 78% of TC could still be removed from the system within 10 min, which reflects the strong adaptability of the CoCu10/PMS process.

The above speculation was also be confirmed by DFT calculations, and the adsorption configurations and adsorption energies of CoCu10 for six anions are shown in Figs. 8g and 8h. According to the adsorption energy, the adsorption order of the six anions on CoCu10 is $\text{SO}_4^{2-} > \text{H}_2\text{PO}_4^- > \text{HSO}_5^- > \text{HCO}_3^- > \text{NO}_3^- > \text{Cl}^-$. In other words, in the competition for the active sites, HSO_5^- was disadvantaged compared with SO_4^{2-} and H_2PO_4^- , and was dominant compared with the remaining anions. Since Co(IV) would not be consumed by anions, the inhibition of SO_4^{2-} and H_2PO_4^- on the system was due to the excessive occupation of the active sites of CoCu10 by these anions or their ionized products.

To evaluate the performance of the CoCu10/PMS process in real saline wastewater, reef salt (a mixed salt, the composition was shown in Table S3) was used to simulate real saline wastewater. As shown in Fig. 8f, the CoCu10/PMS system exhibited unparalleled performance under salt stress, and the salinity less than 1 wt% had no effect on the TC removal. Interestingly, it was observed that the degradation of TC in the system was accelerated when the salinity exceeded 3 wt%. Reports have suggested that the reaction between high concentrations of Cl^- and PMS could generate HOCl, which possesses strong oxidation capabilities and could accelerate the removal of organic pollutants. However, the acceleration was not observed in the presence of 250 mM Cl^- (Fig. 8a), thus excluding HOCl as the reason for the accelerated degradation of TC. A more plausible explanation is that the reef salt we used contains not only various anions but also different cations such as Ca^{2+} and Mg^{2+} . It has been reported that these cations, with their higher hydration shell thickness, could play a bridging role between HSO_5^- and metal oxides, facilitating the formation of PMS-metal complexes[75,76]. Undoubtedly, the rapid formation of complexes is beneficial for the degradation of pollutants in the CoCu10/PMS system. The stability of CoCu10 in the saline environment is also excellent, as illustrated in Fig. S29, the salinity of 0.5 wt% did not exacerbate metal leaching. After the reaction, the concentrations of Co and Cu in the system were 26.6 $\mu\text{g/L}$ and 812.4 $\mu\text{g/L}$, respectively, which still conform to the relevant standards and would not pose potential environmental risks. At this salinity, the recycling performance of CoCu10 decreased slightly (Fig. S30), which may be due to anions occupying part of its active sites. However, CoCu10 can still maintain a high tetracycline removal rate of 82.8% within 10 min at the fifth cycle, while CoOOH was only 36.2%, which reflects the excellent salt resistance of CoCu10.

During the TC oxidation process, it is possible that intermediate products with higher or lower toxicity might be generated, leading to changes in the toxicity of the reactants[77]. In the saline environment, the presence of halogen elements could potentially result in the formation of halogenated organics, further exacerbating the toxicity of the reactants. To investigate changes in the toxicity of reactants in the CoCu10 or CoOOH/PMS systems, the activated sludge inhibition

experiment was conducted (Fig. S31). It is evident that the oxygen uptake inhibition rates (I_{OUR}) in both systems exhibited an initial increase followed by a subsequent decrease. In the CoCu10/PMS system, the I_{OUR} peaks at 5 min, while the CoOOH/PMS system, due to its comparatively inferior performance, displayed a relatively delayed overall trend. In the early stage of the reaction, although TOC decreased, the I_{OUR} increased, which indicated the formation of intermediate products with increased biotoxicity in the reaction system. However, as the reaction progresses, the I_{OUR} in both systems descended to levels lower than that of TC, which facilitates subsequent biological treatment processes.

Additionally, ciprofloxacin (CIP), rhodamine B (RhB), congo red (CR), methylparaben (MeP), bisphenol A (BPA) together with TC used above were chosen as the target pollutants for assessing the performance of the CoCu10/PMS process at varying salinity levels. As depicted in Fig. S32, under salt-free conditions, all pollutants could be rapidly degraded in the CoCu10/PMS system. Specifically, TC, RhB, CR, MeP, and BPA were completely degraded within 20 min, while the CIP degradation also reached 97% within 40 min. These results highlight the wide-ranging capability of the CoCu10/PMS process. On the other hand, low salinity (0.1 wt%) only resulted in a negligible inhibition on the degradation of TC, CIP, MeP and BPA, without causing substantial effect on the degradation of these pollutants. On the contrary, the degradation of RhB and CR were accelerated, which could be attributed to the bridging effect of the aforementioned cations as discussed above. Additionally, high salinity (1 wt%) also did not inhibit the degradation of these pollutants. Specifically, the degradation of TC and BPA were hardly affected, while the degradation of CIP, RhB, CR and MeP was significantly accelerated due to the bridging effect of cations under high salinity conditions. Finally, the performance of the CoCu10/PMS process was assessed in various real water samples. As depicted in Fig. S33, the degradation of TC by CoCu10/PMS was hardly inhibited in both tap water and lake water. In summary, these findings demonstrate the advantages of the selectivity of Co(IV)=O in the face of complex water matrices and highlight the potential of the CoCu10/PMS process for real water treatment applications.

4. Conclusion

This work used a simple co-precipitation method to prepare Cu-doped CoOOH. The catalyst activates PMS and generates a large amount of Co(IV)=O, which mainly contributed to the degradation of TC. Thanks to Co(IV)=O, CoCu10/PMS system showed high resistance to anions such as Cl^- , HCO_3^- , NO_3^- , SO_4^{2-} and H_2PO_4^- . The CoCu10/PMS process also showed strong degradation of various organic pollutants under different salinity levels. The surface hydroxyls were identified as sites for PMS activation and TC adsorption. These changes jointly enhanced the activation performance of CoCu10/PMS to PMS. This work demonstrates that Co(IV)=O generated in CoCu10/PMS exhibited strong resistance to salt, which is an effective strategy for degrading organic pollutants in saline environments.

CRediT authorship contribution statement

YuFei Han: Conceptualization, Data curation, Investigation, Methodology, Writing – original draft preparation. **Chuanfu Zhao:** Writing – review & editing. **Wenchao Zhang:** Data curation. **Zhe Liu:** Writing – review & editing. **Zhe Li:** Writing – review & editing. **Fei Han:** Writing – review & editing. **Mengru Zhang:** Writing – review & editing. **Fei Xu:** Writing – review & editing. **Weizhi Zhou:** Supervision, Project administration, Writing – review & editing, Funding acquisition.

Declaration of Competing Interest

The authors declare that they have no known competing financial interests or personal relationships that could have appeared to influence the work reported in this paper.

Acknowledgements

This work was supported by the National Natural Science Foundation of China (U1906221); National Key Research and Development Program (2022YFC2807503); Major Program of Shandong Province Technological Innovation Project (2020CXGC011403); Open Research Fund Program of Shandong Provincial Key Laboratory of Oilfield Produced Water Treatment and Environmental Pollution Control (SPE-P2021590). We sincerely appreciate the valuable suggestions provided by anonymous reviewers for this work. We also thank Mr. Yankai Li from Shiyanjia Lab (www.shiyanjia.com) for tests of XPS.

Appendix A. Supporting information

Supplementary data associated with this article can be found in the online version at [doi:10.1016/j.apcatb.2023.123224](https://doi.org/10.1016/j.apcatb.2023.123224).

References

- [1] D. Mangla, A. Sharma, S. Ikram, Critical review on adsorptive removal of antibiotics: Present situation, challenges and future perspective, *J. Hazard. Mater.* 425 (2022), 127946.
- [2] Z.-J. Xiao, X.-C. Feng, H.-T. Shi, B.-Q. Zhou, W.-Q. Wang, N.-Q. Ren, Why the cooperation of radical and non-radical pathways in PMS system leads to a higher efficiency than a single pathway in tetracycline degradation, *J. Hazard. Mater.* 424 (2022), 127247.
- [3] X.-C. Feng, Z.-J. Xiao, H.-T. Shi, B.-Q. Zhou, Y.-M. Wang, H.-Z. Chi, X.-H. Kou, N.-Q. Ren, How nitrogen and sulfur doping modified material structure, transformed oxidation pathways, and improved degradation performance in peroxymonosulfate activation, *Environ. Sci. Technol.* 56 (19) (2022) 14048–14058.
- [4] X. Zheng, X. Niu, D. Zhang, M. Lv, X. Ye, J. Ma, Z. Lin, M. Fu, Metal-based catalysts for persulfate and peroxymonosulfate activation in heterogeneous ways: a review, *Chem. Eng. J.* 429 (2022), 132323.
- [5] F. Chen, L.-L. Liu, J.-J. Chen, W.-W. Li, Y.-P. Chen, Y.-J. Zhang, J.-H. Wu, S.-C. Mei, Q. Yang, H.-Q. Yu, Efficient decontamination of organic pollutants under high salinity conditions by a nonradical peroxymonosulfate activation system, *Water Res.* 191 (2021), 116799.
- [6] J. Wang, S. Wang, Effect of inorganic anions on the performance of advanced oxidation processes for degradation of organic contaminants, *Chem. Eng. J.* 411 (2021), 128392.
- [7] B. Chen, J. Jiang, X. Yang, X. Zhang, P. Westerhoff, Roles and knowledge gaps of point-of-use technologies for mitigating health risks from disinfection byproducts in tap water: a critical review, *Water Res.* 200 (2021), 117265.
- [8] M. Kohantebi, G. Moussavi, S. Giannakis, A review of the innovations in metal- and carbon-based catalysts explored for heterogeneous peroxymonosulfate (PMS) activation, with focus on radical vs. non-radical degradation pathways of organic contaminants, *Chem. Eng. J.* 411 (2021), 127957.
- [9] Y. Bao, C. Lian, K. Huang, H. Yu, W. Liu, J. Zhang, M. Xing, Generating high-valent iron-oxo=FeIV=O complexes in neutral microenvironments through peroxymonosulfate activation by Zn-Fe layered double hydroxides, *Angew. Chem. Int. Ed.* 61 (42) (2022), e202209542.
- [10] J.P. Biswas, S. Guin, D. Maiti, Highvalent 3d metal-oxo mediated C-H halogenation: biomimetic approaches, *Coord. Chem. Rev.* 408 (2020), 213174.
- [11] E. Andris, R. Navrátil, J. Jašek, M. Srnec, M. Rodriguez, M. Costas, J. Roithová, M-O bonding beyond the oxo wall: spectroscopy and reactivity of cobalt (III)-oxyl and cobalt (III)-oxo complexes, *Angew. Chem. Int. Ed.* 58 (28) (2019) 9619–9624.
- [12] A. Ansari, Theoretical insights for generation of terminal metal-oxo species and involvement of the “oxo wall”, *New J. Chem.* 46 (34) (2022) 16269–16272.
- [13] V.A. Larson, B. Battistella, K. Ray, N. Lehnert, W. Nam, Iron and manganese oxo complexes, oxo wall and beyond, *Nat. Rev. Chem.* 4 (8) (2020) 404–419.
- [14] Y. Zong, X. Guan, J. Xu, Y. Feng, Y. Mao, L. Xu, H. Chu, D. Wu, Unraveling the overlooked involvement of high-valent cobalt-oxo species generated from the cobalt (II)-activated peroxymonosulfate process, *Environ. Sci. Technol.* 54 (24) (2020) 16231–16239.
- [15] J. Jiang, Z. Zhao, J. Gao, T. Li, M. Li, D. Zhou, S. Dong, Nitrogen vacancy-modulated peroxymonosulfate nonradical activation for organic contaminant removal via high-valent cobalt-oxo species, *Environ. Sci. Technol.* 56 (9) (2022) 5611–5619.
- [16] K. Qian, H. Chen, W. Li, Z. Ao, Y.-N. Wu, X. Guan, Single-atom Fe catalyst outperforms its homogeneous counterpart for activating peroxymonosulfate to achieve effective degradation of organic contaminants, *Environ. Sci. Technol.* 55 (10) (2021) 7034–7043.
- [17] P. He, C. Gu, B. Tang, Y. Zhou, M. Gan, J. Zhu, Expedited degradation of SMX by high-valent cobalt-oxo species derived from cobalt-doped C3N5-activated peroxymonosulfate with the assistance of visible light, *Sep. Purif. Technol.* 301 (2022), 122009.
- [18] N. Yao, G. Wang, H. Jia, J. Yin, H. Cong, S. Chen, W. Luo, Intermolecular energy gap-induced formation of high-valent cobalt species in CoOOH surface layer on cobalt sulfides for efficient water oxidation, *Angew. Chem.* 134 (28) (2022), e202117178.
- [19] W.H. Lee, M.H. Han, Y.-J. Ko, B.K. Min, K.H. Chae, H.-S. Oh, Electrode reconstruction strategy for oxygen evolution reaction: maintaining Fe-CoOOH phase with intermediate-spin state during electrolysis, *Nat. Commun.* 13 (1) (2022) 605.
- [20] F. Reikowski, F. Maroun, I. Pacheco, T. Wiegmann, P. Allongue, J. Stettner, O. M. Magnussen, Operando surface X-ray diffraction studies of structurally defined Co3O4 and CoOOH thin films during oxygen evolution, *ACS Catalysis* 9 (5) (2019) 3811–3821.
- [21] T. Binninger, R. Mohamed, K. Waltar, E. Fabbri, P. Levecque, R. Kötz, T.J. Schmidt, Thermodynamic explanation of the universal correlation between oxygen evolution activity and corrosion of oxide catalysts, *Sci. Rep.* 5 (1) (2015) 12167.
- [22] C. Cheng, W. Ren, F. Miao, X. Chen, X. Chen, H. Zhang, Generation of FeIV=O and its contribution to fenton-like reactions on a single-atom iron–N–C catalyst, *Angew. Chem. Int. Ed.* 62 (10) (2023), e202218510.
- [23] W. Ren, C. Cheng, P. Shao, X. Luo, H. Zhang, S. Wang, X. Duan, Origins of electron-transfer regime in persulfate-based nonradical oxidation processes, *Environ. Sci. Technol.* 56 (1) (2022) 78–97.
- [24] M. Xiong, B. Chai, G. Fan, X. Zhang, C. Wang, G. Song, Immobilization CoOOH nanosheets on biochar for peroxymonosulfate activation: Built-in electric field mediated radical and non-radical pathways, *J. Colloid Interface Sci.* 638 (2023) 412–426.
- [25] Y. Han, Z. Li, M. Zhang, F. Han, Z. Liu, W. Zhou, Isomorphic substitution of goethite by cobalt: Effects on the pathway and performance of peroxymonosulfate activation, *Chem. Eng. J.* 450 (2022), 138460.
- [26] S.H. Ye, Z.X. Shi, J.X. Feng, Y.X. Tong, G.R. Li, Activating CoOOH porous nanosheet arrays by partial iron substitution for efficient oxygen evolution reaction, *Angew. Chem. Int. Ed.* 57 (10) (2018) 2672–2676.
- [27] L. Yan, B. Zhang, Z. Liu, J. Zhu, Synergy of copper doping and oxygen vacancies in porous CoOOH nanoplates for efficient water oxidation, *Chem. Eng. J.* 405 (2021), 126198.
- [28] B. Lin, A. Wang, Y. Guo, Y. Ding, W. Zhan, L. Wang, Y. Guo, F. Gao, Elimination of NO pollutant in semi-enclosed spaces over sodium-promoted cobalt oxyhydroxide (CoOOH) by oxidation and adsorption mechanism, *Appl. Catal. B: Environ.* 279 (2020), 119404.
- [29] R. Chong, Z. Wang, J. Lv, J. Rong, L. Zhang, Y. Jia, L. Wang, Z. Chang, X. Wang, A hybrid CoOOH-rGO/Fe2O3 photoanode with spatial charge separation and charge transfer for efficient photoelectrochemical water oxidation, *J. Catal.* 399 (2021) 170–181.
- [30] L. Wang, Y. Ni, X. Hou, L. Chen, F. Li, J. Chen, A two-dimensional metal–organic polymer enabled by robust nickel–nitrogen and hydrogen bonds for exceptional sodium-ion storage, *Angew. Chem. Int. Ed.* 59 (49) (2020) 22126–22131.
- [31] J. Ren, J. Li, L. Lv, J. Wang, Degradation of caffeine acid by dielectric barrier discharge plasma combined with Ce doped CoOOH catalyst, *J. Hazard. Mater.* 402 (2021), 123772.
- [32] X. Xu, H. Liu, J. Wang, T. Chen, X. Ding, H. Chen, Insight into surface hydroxyl groups for environmental purification: characterizations, applications and advances, *Surf. Interfaces* 25 (2021), 101272.
- [33] Y. Zhao, H. An, J. Feng, Y. Ren, J. Ma, Impact of crystal types of AgFeO2 nanoparticles on the peroxymonosulfate activation in the water, *Environ. Sci. Technol.* 53 (8) (2019) 4500–4510.
- [34] D. Liu, Z. Su, B. Han, K. Xia, C. Zhou, Q. Gao, Cobalt–aluminum oxide clusters-embedded γ-Al2O3 nanosheets for peroxymonosulfate activation: Interfacial pH-buffering property to eliminate cobalt leaching and boost the catalytic activity, *Appl. Catal. B: Environ.* 330 (2023), 122555.
- [35] T. Ghodselahi, M. Vesaghi, A. Shafeekhani, A. Baghizadeh, M. Lameii, XPS study of the Cu@Cu2O core-shell nanoparticles, *Appl. Surf. Sci.* 255 (5) (2008) 2730–2734.
- [36] M. Donohue, G. Aranovich, Adsorption hysteresis in porous solids, *J. Colloid Interface Sci.* 205 (1) (1998) 121–130.
- [37] L. Wu, Z. Sun, Y. Zhen, S. Zhu, C. Yang, J. Lu, Y. Tian, D. Zhong, J. Ma, Oxygen vacancy-induced nonradical degradation of organics: critical trigger of oxygen (O2) in the Fe–Co LDH/peroxymonosulfate system, *Environ. Sci. Technol.* 55 (22) (2021) 15400–15411.
- [38] H. Chen, Y. Xu, K. Zhu, H. Zhang, Understanding oxygen-deficient La2CuO4-δ perovskite activated peroxymonosulfate for bisphenol A degradation: the role of localized electron within oxygen vacancy, *Appl. Catal. B: Environ.* 284 (2021), 119732.
- [39] Y. Bao, W.-D. Oh, T.-T. Lim, R. Wang, R.D. Webster, X. Hu, Elucidation of stoichiometric efficiency, radical generation and transformation pathway during catalytic oxidation of sulfamethoxazole via peroxymonosulfate activation, *Water Res.* 151 (2019) 64–74.
- [40] I. Othman, J.H. Zain, M.A. Haija, F. Banat, Catalytic activation of peroxymonosulfate using CeVO4 for phenol degradation: an insight into the reaction pathway, *Appl. Catal. B: Environ.* 266 (2020), 118601.
- [41] W. Hu, L. Yang, P. Shao, H. Shi, Z. Chang, D. Fang, Y. Wei, Y. Feng, Y. Huang, K. Yu, Proton self-enhanced hydroxyl-enriched cerium oxide for effective arsenic extraction from strongly acidic wastewater, *Environ. Sci. Technol.* 56 (14) (2022) 10412–10422.
- [42] H. Zheng, J. Bao, Y. Huang, L. Xiang, B. Ren, J. Du, M.N. Nadagouda, D. Dionysiou, Efficient degradation of atrazine with porous sulfurized Fe2O3 as catalyst for peroxymonosulfate activation, *Appl. Catal. B: Environ.* 259 (2019), 118056.
- [43] X. Xu, S. Zong, W. Chen, D. Liu, Heterogeneously catalyzed binary oxidants system with magnetic fly ash for the degradation of bisphenol A, *Chem. Eng. J.* 360 (2019) 1363–1370.

[44] W. Li, X. He, B. Li, B. Zhang, T. Liu, Y. Hu, J. Ma, Structural tuning of multishelled hollow microspheres for boosted peroxyomonosulfate activation and selectivity: role of surface superoxide radical, *Appl. Catal. B: Environ.* 305 (2022), 121019.

[45] S. She, J. Wang, J. Liu, C. Gao, Y. Li, L. Yang, X. Wu, S. Song, Reusing warm-paste waste as catalyst for peroxyomonosulfate activation toward antibiotics degradation under high salinity condition: Performance and mechanism study, *Chem. Eng. J.* 426 (2021), 131295.

[46] C. Liang, H. Sun, C. Ling, X. Liu, M. Li, X. Zhang, F. Guo, X. Zhang, Y. Shi, S. Cao, Pyrolysis temperature-switchable Fe-N sites in pharmaceutical sludge biochar toward peroxyomonosulfate activation for efficient pollutants degradation, *Water Res.* 228 (2023), 119328.

[47] Z. Wang, B. Liu, C. Ji, L. Tang, B. Huang, L. Feng, Y. Feng, Insight into electrochemically boosted trace Co (II)-PMS catalytic process: sustainable Co (IV)/Co (III)/Co (II) cycling and side reaction blocking, *J. Hazard. Mater.* 448 (2023), 130905.

[48] J. Pan, B. Gao, P. Duan, K. Guo, M. Akram, X. Xu, Q. Yue, Y. Gao, Improving peroxyomonosulfate activation by copper ion-saturated adsorbent-based single atom catalysts for the degradation of organic contaminants: electron-transfer mechanism and the key role of Cu single atoms, *J. Mater. Chem. A* 9 (19) (2021) 11604–11613.

[49] E.-T. Yun, J.H. Lee, J. Kim, H.-D. Park, J. Lee, Identifying the nonradical mechanism in the peroxyomonosulfate activation process: singlet oxygenation versus mediated electron transfer, *Environ. Sci. Technol.* 52 (12) (2018) 7032–7042.

[50] Y. Zong, L. Chen, Y. Zeng, J. Xu, H. Zhang, X. Zhang, W. Liu, D. Wu, Do we appropriately detect and understand singlet oxygen possibly generated in advanced oxidation processes by electron paramagnetic resonance spectroscopy? *Environ. Sci. Technol.* 57 (25) (2023) 9394–9404.

[51] Y. Wen, V.K. Sharma, X. Ma, Activation of peroxyomonosulfate by phosphate and carbonate for the abatement of atrazine: roles of radical and nonradical species, *ACS ES&T Water* 2 (4) (2022) 635–643.

[52] K.Z. Huang, H. Zhang, Direct electron-transfer-based peroxyomonosulfate activation by iron-doped manganese oxide (6-MnO₂) and the development of galvanic oxidation processes (GOPs), *Environ. Sci. Technol.* 53 (21) (2019) 12610–12620.

[53] P. Duan, J. Pan, W. Du, Q. Yue, B. Gao, X. Xu, Activation of peroxyomonosulfate via mediated electron transfer mechanism on single-atom Fe catalyst for effective organic pollutants removal, *Appl. Catal. B: Environ.* 299 (2021), 120714.

[54] Y. Wei, J. Miao, J. Ge, J. Lang, C. Yu, L. Zhang, P.J. Alvarez, M. Long, Ultrahigh peroxyomonosulfate utilization efficiency over CuO nanosheets via heterogeneous Cu (III) formation and preferential electron transfer during degradation of phenols, *Environ. Sci. Technol.* 56 (12) (2022) 8984–8992.

[55] Y. Zong, H. Zhang, X. Zhang, W. Liu, L. Xu, D. Wu, High-valent cobalt-oxo species triggers hydroxyl radical for collaborative environmental decontamination, *Appl. Catal. B: Environ.* 300 (2022), 120722.

[56] J. Song, N. Hou, X. Liu, M. Antonietti, P. Zhang, R. Ding, L. Song, Y. Wang, Y. Mu, Asymmetrically coordinated CoB1N3 moieties for selective generation of high-valence co-oxo species via coupled electron–proton transfer in fenton-like reactions, *Adv. Mater.* 35 (23) (2023) 2209552.

[57] J. Song, N. Hou, X. Liu, M. Antonietti, Y. Wang, Y. Mu, Unsaturated single-atom CoN₃ sites for improved fenton-like reaction towards high-valent metal species, *Appl. Catal. B: Environ.* 325 (2023), 122368.

[58] T. Zhang, H. Zhu, J.-P. Croué, Production of sulfate radical from peroxyomonosulfate induced by a magnetically separable CuFe2O4 spinel in water: efficiency, stability, and mechanism, *Environ. Sci. Technol.* 47 (6) (2013) 2784–2791.

[59] G.-X. Huang, C.-Y. Wang, C.-W. Yang, P.-C. Guo, H.-Q. Yu, Degradation of bisphenol A by peroxyomonosulfate catalytically activated with Mn1.8Fe1.2O4 nanospheres: synergism between Mn and Fe, *Environ. Sci. Technol.* 51 (21) (2017) 12611–12618.

[60] P. Duan, X. Liu, B. Liu, M. Akram, Y. Li, J. Pan, Q. Yue, B. Gao, X. Xu, Effect of phosphate on peroxyomonosulfate activation: accelerating generation of sulfate radical and underlying mechanism, *Appl. Catal. B: Environ.* 298 (2021), 120532.

[61] S. Wu, H. Li, X. Li, H. He, C. Yang, Performances and mechanisms of efficient degradation of atrazine using peroxyomonosulfate and ferrate as oxidants, *Chem. Eng. J.* 353 (2018) 533–541.

[62] Q. Zhang, D. He, X. Li, W. Feng, C. Lyu, Y. Zhang, Mechanism and performance of singlet oxygen dominated peroxyomonosulfate activation on CoOOH nanoparticles for 2, 4-dichlorophenol degradation in water, *J. Hazard. Mater.* 384 (2020), 121350.

[63] M. Huang, Y.-S. Li, C.-Q. Zhang, C. Cui, Q.-Q. Huang, M. Li, Z. Qiang, T. Zhou, X. Wu, H.-Q. Yu, Facilely tuning the intrinsic catalytic sites of the spinel oxide for peroxyomonosulfate activation: From fundamental investigation to pilot-scale demonstration, *Proc. Natl. Acad. Sci. USA* 119 (30) (2022), e2202682119.

[64] S. Shen, X. Zhou, Q. Zhao, W. Jiang, J. Wang, L. He, Y. Ma, L. Yang, Z. Chen, Understanding the nonradical activation of peroxyomonosulfate by different crystallographic MnO₂: The pivotal role of MnIII content on the surface, *J. Hazard. Mater.* 439 (2022), 129613.

[65] H. Sun, F. He, W. Choi, Production of reactive oxygen species by the reaction of periodate and hydroxylamine for rapid removal of organic pollutants and waterborne bacteria, *Environ. Sci. Technol.* 54 (10) (2020) 6427–6437.

[66] Y. Rao, Y. Zhang, J. Fan, G. Wei, D. Wang, F. Han, Y. Huang, J.-P. Croué, Enhanced peroxyomonosulfate activation by Cu-doped LaFeO₃ with rich oxygen vacancies: compound-specific mechanisms, *Chem. Eng. J.* 435 (2022), 134882.

[67] L. Long, L. Su, W. Hu, S. Deng, C. Chen, F. Shen, M. Xu, G. Huang, G. Yang, Micro-mechanism of multi-pathway activation peroxyomonosulfate by copper-doped cobalt silicate: the dual role of copper, *Appl. Catal. B: Environ.* 309 (2022), 121276.

[68] F. Mo, C. Song, Q. Zhou, W. Xue, S. Ouyang, Q. Wang, Z. Hou, S. Wang, J. Wang, The optimized Fenton-like activity of Fe single-atom sites by Fe atomic clusters-mediated electronic configuration modulation, *Proc. Natl. Acad. Sci. USA* 120 (15) (2023), e2300281120.

[69] H. Chi, X. He, J. Zhang, D. Wang, X. Zhai, J. Ma, Hydroxylamine enhanced degradation of naproxen in Cu²⁺ activated peroxyomonosulfate system at acidic condition: efficiency, mechanisms and pathway, *Chem. Eng. J.* 361 (2019) 764–772.

[70] X. Zhou, H. Luo, B. Sheng, X. Chen, Y. Wang, Q. Chen, J. Zhou, Cu²⁺/Cu⁺ cycle promoted PMS decomposition with the assistance of Mo for the degradation of organic pollutant, *J. Hazard. Mater.* 411 (2021), 125050.

[71] Z. Wu, Y. Wang, Z. Xiong, Z. Ao, S. Pu, G. Yao, B. Lai, Core-shell magnetic Fe3O₄@Zn/Co-ZIFs to activate peroxyomonosulfate for highly efficient degradation of carbamazepine, *Appl. Catal. B: Environ.* 277 (2020), 119136.

[72] J. Lu, Y. Zhou, Y. Zhou, Efficiently activate peroxyomonosulfate by Fe3O₄@MoS₂ for rapid degradation of sulfonamides, *Chem. Eng. J.* 422 (2021), 130126.

[73] Y. Ji, C. Dong, D. Kong, J. Lu, New insights into atrazine degradation by cobalt catalyzed peroxyomonosulfate oxidation: kinetics, reaction products and transformation mechanisms, *J. Hazard. Mater.* 285 (2015) 491–500.

[74] H. Watanabe, C.D. Gutleben, Je Seto, Sulfate ions on the surface of maghemite and hematite, *Solid State Ion.* 69 (1) (1994) 29–35.

[75] L. Wang, J. Jiang, S.-Y. Pang, Y. Zhou, J. Li, S. Sun, Y. Gao, C. Jiang, Oxidation of bisphenol A by nonradical activation of peroxyomonosulfate in the presence of amorphous manganese dioxide, *Chem. Eng. J.* 352 (2018) 1004–1013.

[76] S. Allard, L. Gutierrez, C. Fontaine, J.-P. Croué, H. Gallard, Organic matter interactions with natural manganese oxide and synthetic birnessite, *Sci. Total Environ.* 583 (2017) 487–495.

[77] Z.-J. Xiao, B.-Q. Zhou, X.-C. Feng, H.-T. Shi, Y.-N. Zhu, C.-P. Wang, B. Van der Bruggen, N.-Q. Ren, Anchored Co-oxo generated by cobalt single atoms outperformed aqueous species from the counterparts in peroxyomonosulfate treatment, *Appl. Catal. B: Environ.* 328 (2023), 122483.